Version of Record: https://www.sciencedirect.com/science/article/pii/S1359431123014928
Manuscript_9b1040586a8b3450e6d2a43869e9d8e8

Investigation of ice detachment by a liquid jet on various submerged surfaces for the development of ice slurry generators without mechanical scraping

Walid SAMAH [1, 2, *], Pascal CLAIN [1, 2], François RIOUAL [2], Laurence FOURNAISON [2] and Anthony DELAHAYE [2].

[1] Leonard de Vinci Pôle Universitaire, Research Center, 92916 Paris La Défense, France.
[2] Université Paris-Saclay, INRAE, FRISE, 92761 Antony, France.
* Corresponding author: Walid SAMAH, walid.samah@inrae.fr, postal address: INRAE, FRISE, 1 Rue Pierre Gilles de Gennes, 92160 Antony, France.

Abstract: Ice slurry is an alternative method to reduce the quantity and emission of greenhouse refrigerants, as well as control electrical energy consumption. However, the production of ice slurry requires the use of scraped-surface generators, which are costly to maintain and consume high mechanical energy. Therefore, studying the icephobic behavior of surfaces is of interest to significantly reduce ice adhesion and facilitate detachment without the need for mechanical scrapers. This study focuses on the growth, adhesion, and detachment phenomena of ice by liquid jets on different types of surfaces (hydrophilic, hydrophobic, and superhydrophobic) immersed in a 10 wt.% ethanol/water mixture. A liquid jet is used to detach the ice layer from the surfaces, with a velocity ranging from 0 to 2.87 m s^{-1}, and the surface temperature varies from 25 °C to approximately –9 °C. The results show that ice adheres less to hydrophilic and hydrophobic surfaces compared to superhydrophobic surfaces. The use of PTFE-treated aluminum surfaces (hydrophobic) reduces the required flow velocity to detach the ice layer by half compared to untreated aluminum surfaces (hydrophilic). An ANSYS® Fluent numerical model was developed to simulate the evolution of turbulent velocities of immersed liquid jets, and a semi-empirical model was designed to estimate the detachment forces of soft ice from hydrophilic surfaces (untreated aluminum). Two types of ice detachment from surfaces were identified: adhesive detachment and cohesive detachment.

Keywords: Ice slurry generator; Superhydrophobic; Icephobic; Ice adhesion; Ice detachment; Liquid jet.

1. Introduction

The upcoming energy and climate crisis is pushing us to seek new ways to optimize energy while reducing the impact on the environment. This crisis is driven by the increase in global energy consumption, particularly in the refrigeration sector, where electricity consumption represents about 20% of global consumption. Without considering alternative measures, this proportion will continue to rise, especially with global warming. Conventional systems of cold production using refrigerant gases have a significant impact on energy consumption and the environment. Secondary refrigeration offers an effective solution to significantly reduce the amount of refrigerant gas used, as the cold is transported by a neutral fluid called secondary fluid to the place of use. When this secondary fluid contains a phase change material (PCM) [1–3], such as suspended ice particles (ice slurry), electrical energy can be optimized through thermal storage [4–6]. Ice slurries consist of ice particles suspended in an aqueous solution with an average diameter of 1 mm or smaller [7]. Transporting cold using ice slurries is a cost-effective and energy-efficient method because the ice slurry can be stored for extended periods.

There are several technologies for cold storage using ice, including ice harvesting, external ice-on-coil fusion systems, internal ice-on-coil fusion systems, encapsulated ice systems, and ice slurry [8]. These systems, based on Cold Thermal Energy Storage (CTES) using the latent heat of fusion of water (335 kJ kg $^{-1}$), allow storing thermal energy in the form of ice during periods of low cooling demand, to be later released when demand is higher [8–11].

Afsharpanah et al. [9] conducted a numerical study to examine the charging performance of a thermal energy storage device based on ice. This device consists of a small cuboid container equipped with two rows of serpentine tubes with connecting plates. Designed as a backup cooling system for domestic refrigerators in developing countries, this device aims to compensate for thermal load during frequent power outages in those regions and to preserve food during such times.

The authors' [9] study highlights key parameters that influence the charging performance of the ice storage device. The results show that certain dimensions and characteristics of the system can be optimized to improve the charging rate, which could be beneficial for cooling backup applications in developing countries, especially during frequent power outages. These interesting findings pave the way for potential future improvements in the design and use of such domestic energy storage, contributing to better food preservation and increased energy efficiency in refrigeration systems.

Ice slurry is used in many fields such as medical care, the food industry, firefighting, air conditioning [2], and other industrial applications [12].

There are several ice slurry generators, which can be classified into two categories [13,14]:

- Generators with moving components that are directly related to the extraction of ice from the surface (scraped or brushed surface generator) [15] or the transformation of ice blocks into ice slurry by grinding (falling film generator), etc. [13,14].
- Generators without moving parts such as the supercooling generator, direct contact ice slurry generator [16,17], and vacuum ice slurry generator [18], etc. [14].

Most ice slurry generators without moving parts, excluding the ice slurry generator using the supercooling phenomenon, are at the prototype or laboratory study technology readiness level (TRL), with a TRL between 1 and 5 [14]. The most industrially advanced generators with a moving component are scraped or brushed surface generators, while the most advanced generators without a moving component are ice slurry generators that utilize the supercooling phenomenon.

However, these two types of generators have disadvantages:

- The ice slurry generator using the supercooling phenomenon can be blocked because of the uncontrolled breakdown of the supercooling inside the generator, as well as the formation and agglomeration of the ice inside the device, thus resulting in discontinuous production of ice slurry.
- Generators with scraped or brushed surfaces have disadvantages such as low energy efficiency (additional mechanical energy consumption for the rotation of the scrapers) and high maintenance costs due to the wear of the scrapers [14].

To address these drawbacks, researchers working in the refrigeration industry have developed new experimental approaches to optimize ice slurry production without using moving components. These approaches include: the production of ice slurry by hydro scraping with intermittent flow and reduced cooling energy at the time of ice detachment [19], the use of smooth and/or low surface energy materials such as nylon 11 or polytetrafluoroethylene (Teflon® or PTFE) to reduce ice adhesion and facilitate ice detachment by flow [20,21], the use of additives to make the ice morphology softer (porous ice or ice with needle-shaped crystals), resulting in its reduced contact surface with the exchanger walls and thus decreasing its adhesion to the surface [22], and the use of icephobic or superhydrophobic coatings to increase the supercooling degree in supercooling generators [23–30].

However, none of these methods are ready for industrial use, and there is a lack of visual analysis to better understand the phenomenon of ice detachment from surfaces. For example, studies of ice slurry production by hydro scraping in a PTFE or nylon 11 helical tube heat exchanger (HCHX) [20,21], as well as in steel tube heat exchangers [19], have been performed with compact tube heat exchangers that are not transparent. This lack of visibility makes it difficult to establish an empirical or semi-empirical relationship between flow velocity and ice detachment. In addition, these tubular heat exchangers often experience clogging problems due to ice agglomeration in the tubes, making it difficult to study ice detachment. Although Zhao et al. [22] focus on visualization, their study does not provide a complete visualization of ice detachment by flow because it is only based on the decrease in ice thickness, rather than the lengthwise detachment of the ice from the surface. These studies deserve further investigation with the visualization of ice detachment phenomena on the surface by flow (also called hydro-scraping or by the hydrodynamic effect). The variation of flow velocity, surface temperature, and surface states (hydrophilic, hydrophobic, superhydrophobic) are also parameters to consider in order to better understand ice adhesion and detachment phenomena.

The present work is the first study on the ice detachment by a liquid jet with variable velocities on immersed surfaces. The main objective of this study is to understand the phenomena of growth, adhesion, and detachment of ice by flow on different types of surfaces (different wettability and surface conditions). It aims at optimizing the ice slurry production method to develop a new method for ice slurry production without moving components. To achieve these objectives, three types of surfaces (hydrophilic, hydrophobic, and superhydrophobic) were studied in a transparent rectangular device placed on a loop circulating a 10 wt.% ethanol/water mixture. This device is also equipped with a heat exchanger for crystallization and a rectangular nozzle for liquid jet generation. This study focuses on understanding the effect of temperature and surface condition on the growth and detachment of ice on a given surface. Additionally, it examines the effect of increasing liquid jet velocity on ice detachment to select surfaces with less adhesion and seek the most optimal conditions. The originality of this study lies in the visualization of ice growth and detachment phenomena by a liquid jet (flow) on submerged surfaces and in the evaluation of the ice detachment length (L_D) along a surface as a function of the flow velocity. This is done to establish an empirical relationship and to understand the ice detachment phenomena in immersion. Thus, an ANSYS® Fluent numerical model was developed to simulate the evolution of turbulent velocities of immersed liquid jets along the heat exchanger surface for comparison with experimental results.

2. Materials and methods

The objective of this study is to better understand the phenomena of ice adhesion and detachment in immersion on several types of surfaces with different wettability and surface states to develop a new ice slurry generator without moving components. Therefore, two devices were developed. Firstly, a device to measure contact angles (*CA*) on the studied surfaces, and secondly, a device to identify the surfaces that allow optimal ice detachment by shear flow (liquid jet) of a 10 wt.% ethanol/water mixture through a rectangular nozzle. This section is composed of four subsections: the first describes the experimental setups for measuring contact angles; the second describes the experimental setups for the study of ice growth and detachment by flow; the third describes the experimental protocol for the ice detachment setup; and the fourth sub-section describes the numerical model developed using ANSYS Fluent 2021 R1 to simulate the evolution of turbulent liquid jet velocities in immersion. The aim of this simulation is to make a comparison with experimental results and to understand why, at a certain speed, the ice no longer detaches itself from the surface studied. The overall objective is to establish an empirical relationship between jet velocity variation and ice detachment lengths (L_D).

2.1 Experimental set-up for wettability and roughness analysis

An original goniometer was developed for wettability analysis (contact angle measurement) on different surfaces and was presented in detail in a previous work [28]. The device is shown in Figure 1. This goniometer is equipped with a USB CMOS digital microscope camera from Chengstore with 640 x 480 resolution and x1600 zoom, a white light source, an aluminum heat exchanger to maintain the temperature of the samples at a fixed value, and a circulating cryostat bath to control the surface temperature of the heat exchanger. The camera is connected to a computer to measure the contact angle (*CA*) using the IC Measure V2.0.0.286 software. Roughness analysis of the three surface types (hydrophilic, hydrophobic, and superhydrophobic) was performed using a KEYENCE VHX-

7000N/VHX-970N digital microscope. The results of the contact angle and roughness measurements are presented in the results section.

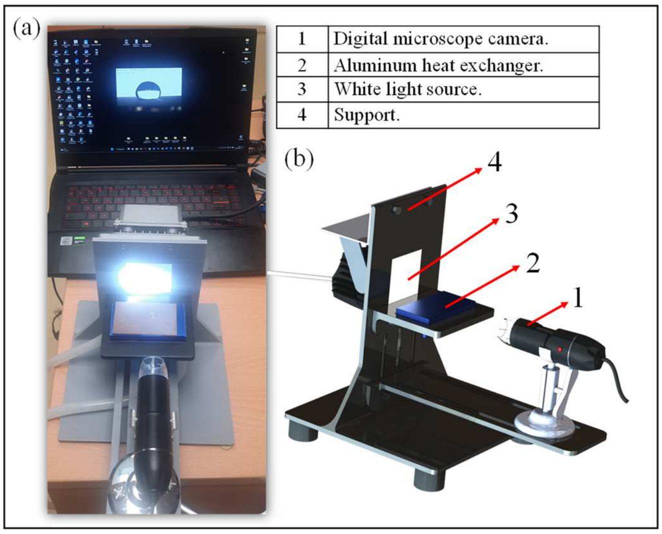

Figure 1 – Contact angle measuring device, (a) real image of the goniometer; (b) design image of the goniometer on SOLIDWORKS.

Three AW1050H24 aluminum surface samples are used to represent different wetting and surface states: hydrophilic, hydrophobic, and superhydrophobic, to characterize their ability to reduce ice adhesion. The first surface is an untreated aluminum surface. The second surface of the same material (aluminum) is treated with a 13 µm thick PTFE adhesive tape from REKALARO. This tape is made of a PTFE-coated fiberglass fabric, which gives it additional properties of tear, tensile, and puncture resistance. The third surface is treated with a commercial superhydrophobic "Ultra Ever Dry" (UED) coating applied in two layers by spraying, the preparation process of which is described in detail in an earlier study [28].

2.2 Experimental device of ice detachment study

To investigate the detachment of the ice layer on the three surfaces described in subsection 2.1, a system was developed for and presented in Figure 2. This system consists of a BEWINNER aluminum heat exchanger (component 8 in Figure 3) with dimensions 0.16 m x 0.04 m x 0.012 m (length, width, height), which is insulated on all sides, except for the top side where the surface samples are fixed with thermal paste. To remove the ice on the surface, a liquid jet is projected onto the surface through an ARIANA flat nozzle (component 9 in Figure 3) with a rectangular (S_N) outlet section measuring 30 mm x 2 mm. The entire system is immersed in a 10 wt.% ethanol/water mixture with an immersion depth of 2 cm between the surface sample and the air/liquid interface. The ice detachment length (L_D) is defined as the maximum distance between the nozzle outlet section and the remaining ice layer on the surface at the furthest point.

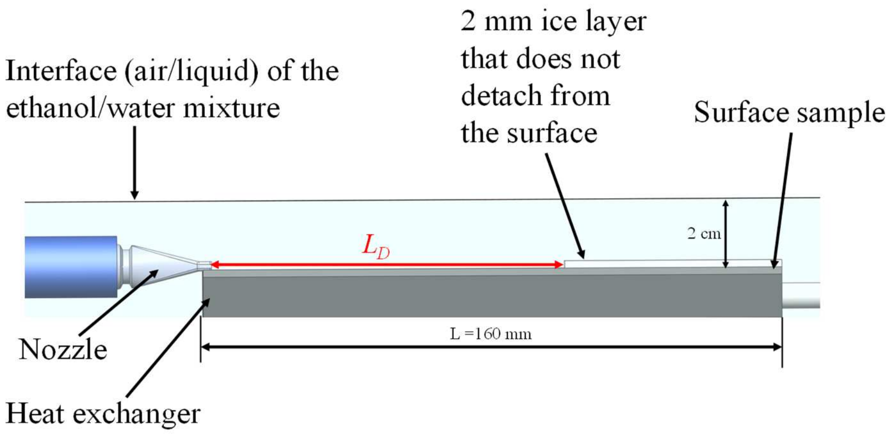

Figure 2 – Schematic representation of the ice detachment length L_D by a liquid jet flow along the surface sample.

The experimental setup shown in Figure 2 is placed in a transparent box made of Polymethylmethacrylate (PMMA), which is identified as component 2 in Figure 3. The dimensions of the box are 0.34 m x 0.146 m x 0.127 m (length, width, height). This entire setup is called the surface testing section, and it includes a high-speed camera (component 7 in Figure 3), specifically the monochrome camera AOS Cesyco PROMON U750, which has a recording speed of 750 frames per second and a KOWA zoom lens with a fixed resolution of 640 x 480. The section viewed by this camera is shown in Figure 3 as a green dashed square, clearly representing the observed region. The video recording of the ice layer formation and its detachment by the flow is performed using the AOS Imaging Studio software version 4.7.2.4. Additionally, a second digital camera is placed above the exchanger to take pictures after the ice detachment (component 1 in Figure 3). The ice detachment length, L_D, is measured using IC Measure software version 2.0.0.286. To remove the dew that forms on the surface of the PMMA box during the cooling of the mixture and for better visualization of the formation and detachment of the ice layer by the liquid jet, a servo motor (component 15 in Figure 3) equipped with a wiper (component 14 in Figure 3) is installed. The servo motor is controlled by an ELEGOO UNO R3 controller board (component 3 in Figure 3), which is programmed to allow the wiper to make a round trip every 4 seconds with an opening angle of 120°. The nozzle is fed by the pump integrated into the circulating cryostat (component III in Figure 4) through a filling tube (components 11 and 10 in Figure 3), with an adjustable mass flow rate from 0 to 0.167 kg s^{-1}. Finally, the PMMA box is continuously fed through a filling tube (component 12 in Figure 3) that connects to an external pump component (component IV in Figure 4) that takes liquid from the circulating cryostat (component III in Figure 4) with a constant mass flow rate of 0.151 kg s^{-1} during experiments.

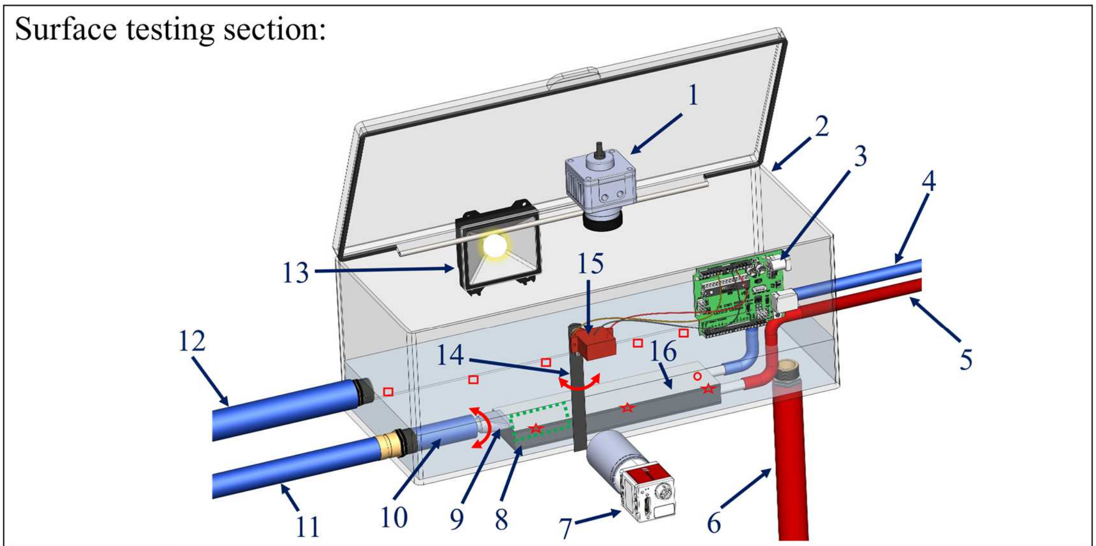

1	Digital camera.
2	Polymethylmethacrylate (PMMA) box 0.34 m x 0.146 m x 0.127 m (length, width, height).
3	ELEGOO UNO R3 controller board.
4	50 wt.% ethanol-water mixture inlet.
5	50 wt.% ethanol-water mixture outlet.
6	Liquid mixture outlet.
7	AOS Cesyco PROMON U750 high speed monochrome camera and KOWA zoom lens . Image resolution 640 x 480
8	Bewinner aluminum heat exchanger 0.16 m x 0.04 m x 0.012 m (length, width, height).
9	ARIANA flat nozzle with 0.03 m x 0.002 m (width, height) outlet section.
10	Nozzle swivel tube.
11	Nozzle supply tube.
12	Filling tube of the PMMA box with the liquid mixture.
13	A-LED LIGHTING 15 Watt.
14	Wiper.
15	Servo motor SG90.
16	Surface sample.

Figure 3 – Detailed schematic of the surface testing section, highlighting its components that make it up (component I of Figure 4)

The measurement of temperatures on the surface testing section is carried out using several T-type thermocouples with a measurement uncertainty of ±0.03 °C. These thermocouples are connected to a KEYSIGHT Model DAQ970A data acquisition system connected to a computer. A thermocouple is placed on the surface sample approximately 150 mm from the nozzle outlet section, shown in Figure 3 by a red circle. The purpose of placing a single thermocouple on the sample surface is to minimize disturbance during ice formation and detachment. Tests were performed to verify the homogeneity of the temperature along the sample surface and the average difference over several points that does not exceed ±0.5 °C. This result validates the use of a single thermocouple on the surface. Three thermocouples are placed between the surface sample (component 16 in Figure 3) and the heat exchanger (component 8 in Figure 3) and are represented in Figure 3 by red stars. Five thermocouples are placed in the surface testing section to measure the temperature of the aqueous mixture at different locations, represented in Figure 3 by red squares.

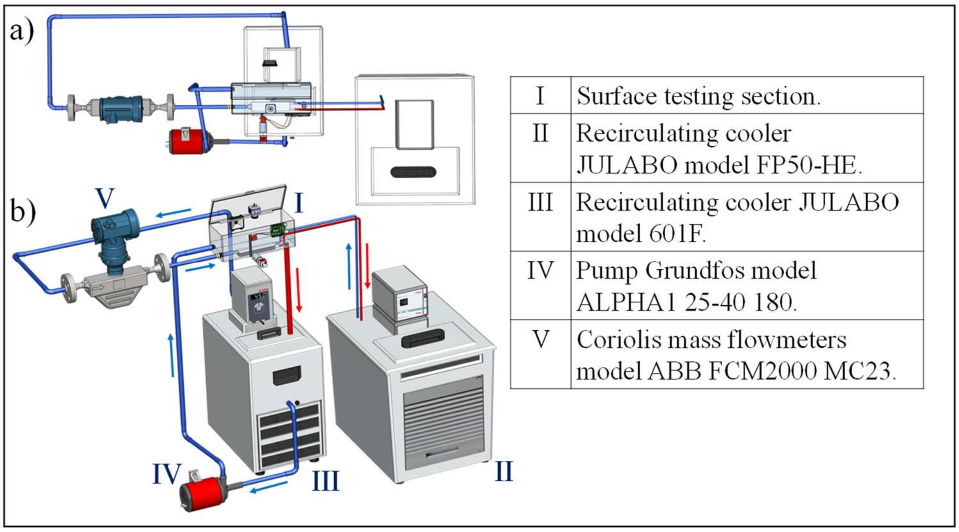

Figure 4 – Schematic of the experimental setup to study ice detachment by flow on different surfaces: (a) top view; (b) perspective view.

Figure 4 shows the complete experimental setup of ice detachment by shear flow. This device is composed of a surface testing section (component I in Figure 4), two circulating cryostats JULABO model FP50-HE (component II in Figure 4) and 601F (component III in Figure 4), a Grundfos pump model ALPHA1 25-40 180 (component IV in Figure 4), and an ABB Coriolis mass flow rate meter model FCM2000 MC23 (component V in Figure 4). The entire setup is placed in a climate chamber at a fixed temperature of 13 °C to improve the efficiency of the two circulating cryostats and for reducing heat losses of the experimental setup.

2.3 Experimental parameters and protocols

The experimental protocol for the study of ice growth and detachment by flow (liquid jet) is as follows: first, the pump (component IV in Figure 4) feeding the surface testing section (system shown in Figure 3) is turned on and set at a mass flow rate of 0.151 kg s^{-1}, establishing a water level of 2 cm above the heat exchanger. Then, a circulation of the aqueous mixture is established at a constant mass flow rate of 0.025 kg s^{-1} through the tube feeding the nozzle. As shown in Figure 5, which represents the evolution of the mass flow rate through the nozzle, as well as the temperature of the aqueous mixture (10 wt.% ethanol/water) and the untreated aluminum surface during cooling.

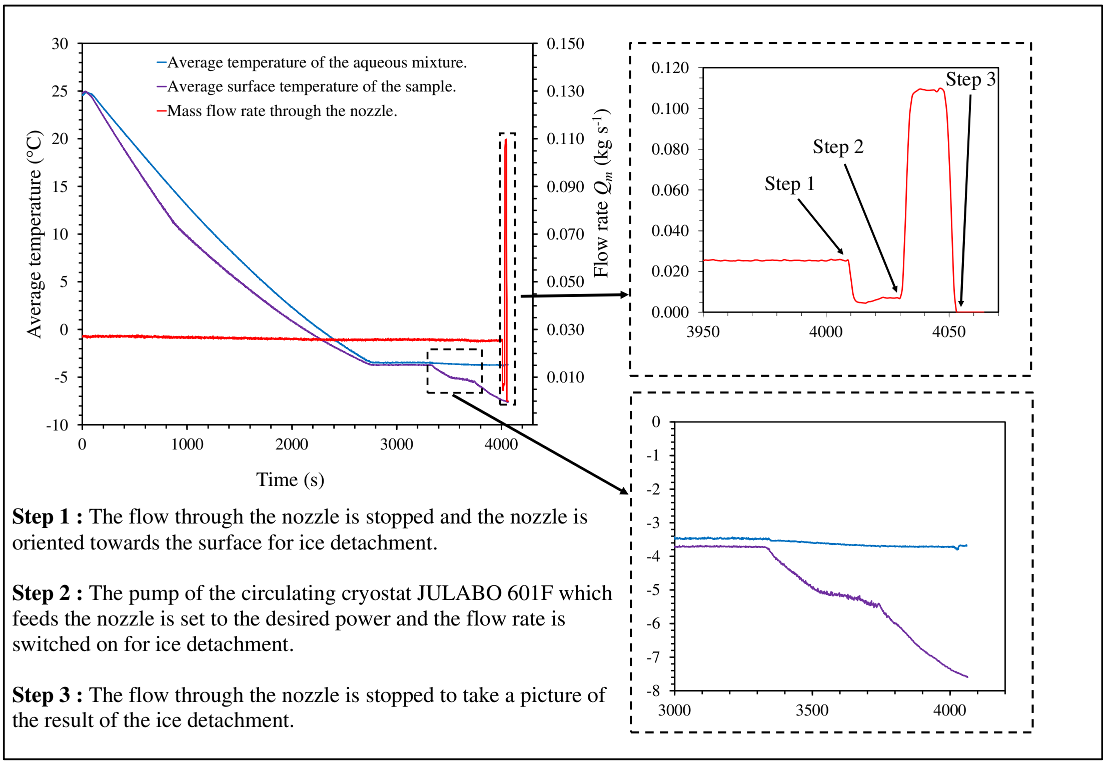

Figure 5– Example of evolution of the mass flow rate through the nozzle and the average temperature of the aqueous mixture (10 wt.% ethanol/water mixture) and the average temperature of the untreated aluminum surface (hydrophilic) during the cooling process.

The purpose of maintaining the flow in the tube feeding the nozzle (components 11 and 10 in Figure 3) is to avoid heating of the liquid mixture at the time of the jet projection for the detachment of the ice layer. Indeed, if the flow is stopped, since the ambient temperature is fixed at 13 °C, heating of the liquid can occur in the tube feeding the nozzle. The nozzle (component 9 in Figure 3) is oriented at about 80° upwards to avoid disturbing the formation of the ice layer. Then, the temperature of the two circulating cryostats (components III and II in Figure 4) that supply the heat exchanger and the surface testing section, respectively, is set to an initial temperature of 25 °C. Then, the temperature of the two circulating cryostats is lowered to achieve stable surface sample and aqueous mixture temperatures at a value of −3.6 °C before crystallization, as shown in Figure 5. Once the surface and liquid mixture temperature are stabilized at −3.6 °C, the sample surface temperature is then lowered to a desired value to initiate crystallization. In the case of Figure 5, the desired surface temperature was −8 °C. Crystallization occurs at the phase change temperature of –4.8 °C to form a 2 mm ice layer on the surface sample immersed in the 10 wt.% ethanol/water mixture, as shown in Figure 6. In Figure 6, the ice layer formation takes about 310 seconds on the untreated aluminum surface. The thickness of the ice layer is set to 2 mm so as not to penalize the heat transfer and to avoid the problem of temperature control.

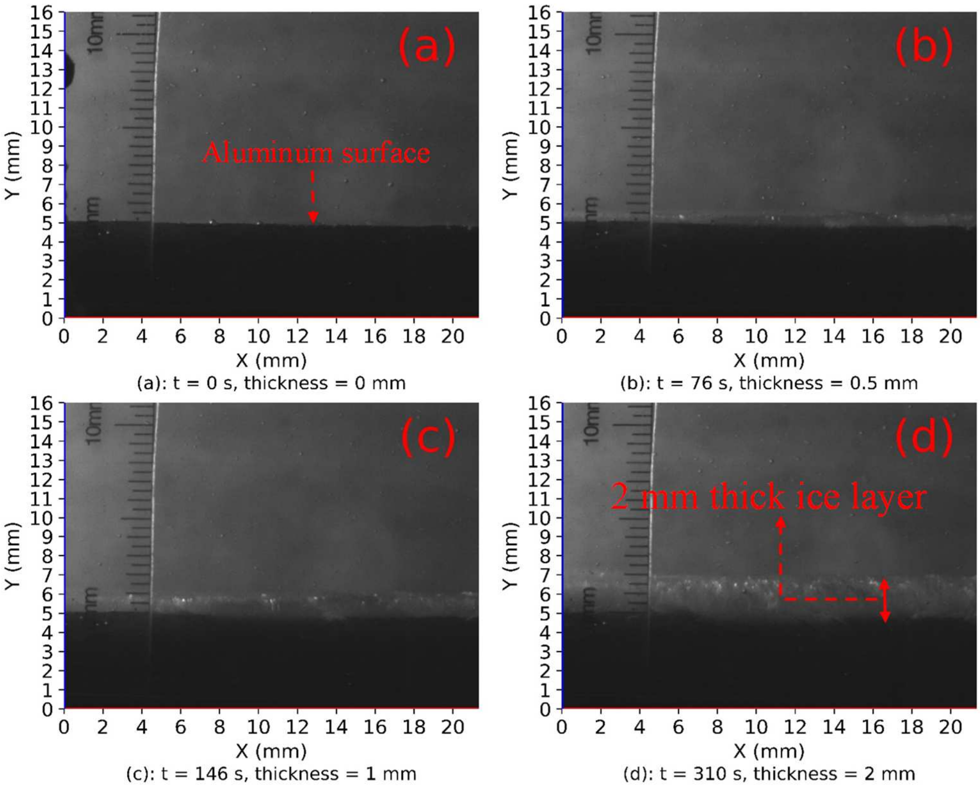

Figure 6 – Evolution of the ice layer thickness that forms on an untreated aluminum surface in a 10 wt.% ethanol/water mixture at a surface temperature set at –8 °C, (a): before crystallization; (d): after crystallization.

During these experiments, temperature and mass flow rate recording through the nozzle are activated using KEYSIGHT software. The high-speed camera (component 7 in Figure 3) is activated to record video of the ice layer formation and its detachment by the flow, and the wiper (component 14 in Figure 3) is turned on to avoid condensation problems. After the ice layer is formed, the flow of the aqueous mixture through the nozzle is stopped, and then the nozzle is directed horizontally towards the surface sample under investigation (downwards) so that the shear flow loosens the ice layer (step 1 in Figure 5). Next, the mass flow rate through the nozzle is adjusted to the desired value (in Figure 5, the set flow rate is 0.109 kg s^{-1}, which corresponds to a flow velocity of 1.83 m s^{-1} at the nozzle outlet), and the flow rate is turned on so that the liquid jet exiting the nozzle loosens the ice layer, as shown in Step 2 of Figure 5. Finally, the filling pump (component IV in Figure 4) and the cryostat circulation pump (component III in Figure 4) are turned off (step 3 in Figure 5) when the ice layer no longer detaches from the surface. A picture of the surface is taken with a camera (component 1 in Figure 3), and the ice detachment length (L_D) is measured using IC Measure image processing software version 2.0.0.286.

2.4 Numerical model for the turbulent jet velocity evolution simulation in immersion

A numerical model is developed to simulate the evolution of the velocity of a turbulent jet in immersion using the ANSYS® FLUENT 2021 R1 software. Several authors have already investigated hydrodynamic phenomena of turbulent liquid jets in immersion, both experimentally and numerically. However, these works do not specifically address the detachment of ice in immersion [31–33]. The objective of our numerical study is to track the evolution of the velocities of the turbulent liquid jet in immersion along the surface of the untreated aluminum sample and does not take account for ice formation and detachment. In our experiment, after the ice detachment, the liquid jet is not immediately stopped; instead, it is allowed to continue for a period of time to ensure that the ice layer no longer detaches and to observe a phenomenon in a steady-state regime. Our simulation hypothesis focuses solely on the evolution of liquid jet velocities over a plane plate within a water-ethanol binary mixture without ice layer, due to the lack of data on ice adhesion forces. The purpose of these simulations is to uncover the reasons behind the detachment of the ice layer at a specific length for each studied velocity, aiming to comprehend the detachment phenomenon. The ultimate goal is to establish a relationship between the experimentally determined ice detachment length (L_D) and the numerically determined maximum turbulent jet length (L_{max}), at which the liquid jet velocity reaches the minimum velocity at which ice detachment does not occur.

The Reynolds number of turbulent liquid jets in these simulations is calculated with equation (Eq.1):

$$R_e = \frac{\rho_l V_N D_H}{\mu} \quad \text{Eq. (1)}$$

Where D_H is the hydraulic diameter of the nozzle, which is 0.00375 m, ρ_l = 983.4 kg m^{-3} is the density of the 10 wt.% ethanol/water mixture at the liquid temperature, which is set at −3.6 °C, V_N is the turbulent velocities at the nozzle outlet (ranging from 1.4 to 2.87 m s^{-1}), and μ = 0.001889 Pa s is the dynamic viscosity of the 10 wt.% ethanol/water mixture at the liquid temperature, which is set at −3.6 °C. The results of the Reynolds number R_e are shown in Table 1. The value of the Reynolds number R_e is greater than 2300, so the velocity of the liquid jet, ranging from 1.4 to 2.87 m s^{-1}, is in the turbulent regime.

Table 1 – Reynolds number of turbulent velocities at the nozzle outlet.

Velocity in nozzle outlet (m s^{-1})	Reynolds R_e (/)
2.87	5545
2.45	4783
2.04	3983
1.87	3651
1.62	3163
1.40	2733

2.4.1 Geometry, boundary conditions and meshing

The fluid domain geometry of the surface testing section (Figure 3) has been modeled using ANSYS® SpaceClaim 3D CAD Modeling Software, as illustrated in Figure 7. The dimensions of the geometry and the specifics of the boundary conditions have also been provided in the same Figure. Table 2 summarizes the boundary conditions that have been defined in the Fluent software. The mesh was created using Fluent mesh software. It is a hybrid mesh consisting of tetrahedral and hexacore meshes, as shown in Figure 8.

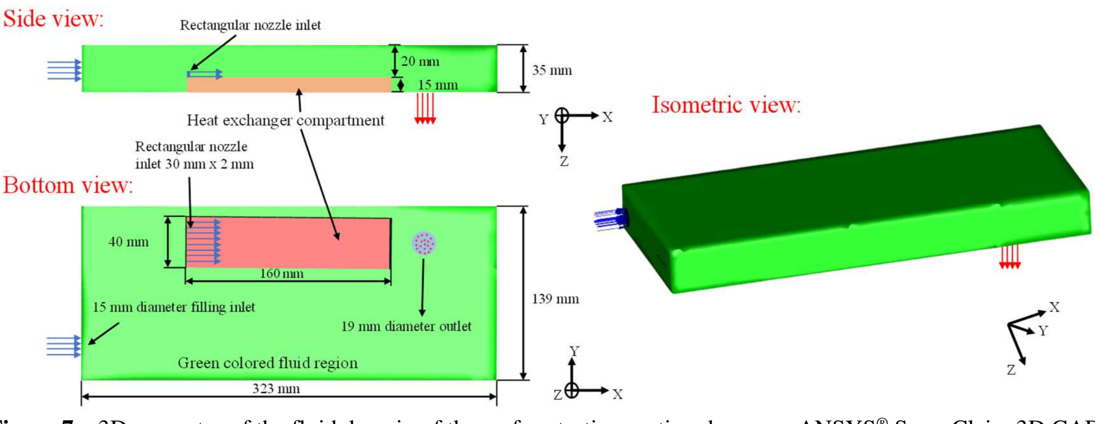

Figure 7 – 3D geometry of the fluid domain of the surface testing section drawn on ANSYS® SpaceClaim 3D CAD Modeling Software.

Table 2 – Boundary conditions declared in the Fluent software.

Positions	Boundary conditions
Filling inlet	Velocity Inlet (inlet velocity fixed at 0.86 m s^{-1} during all simulations).
Rectangular nozzle inlet	Velocity Inlet (The velocities studied range from 1.4 to 2.87 m s^{-1}).
Outlet	Pressure Outlet
Walls	No-slip wall conditions

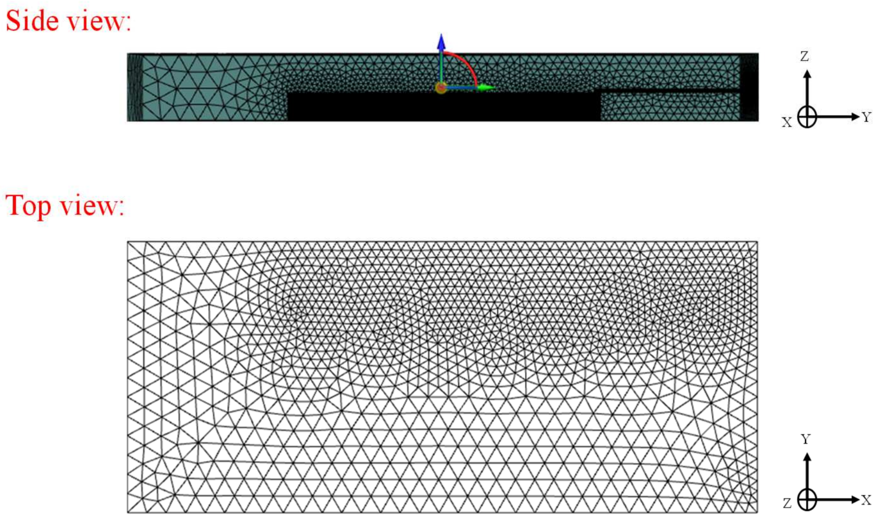

Figure 8 – Fluid domain mesh image of the surface testing section drawn on ANSYS® Fluent meshing software.

2.4.2 Numerical discretizations

The ANSYS® Fluent 2021 R1 software was used to perform a 3D steady-state simulation of a turbulent liquid jet in immersion. The turbulence model chosen was the k-epsilon Realizable with Enhanced Wall Treatment. The Coupled algorithm was used to couple the velocity and pressure. The spatial Second Order discretization scheme was used to discretize the pressure, while First Order Upwind was used for the momentum, turbulent kinetic energy, and turbulent dissipation energy. ANSYS® Fluent's default relaxation values were used for the parameters of pressure, density, body force, and turbulent viscosity, with 0.3 for the momentum and 0.7 for turbulent kinetic energy and turbulent dissipation energy. The computational results were considered convergent when the residual was less than 10^{-6} for all equations and stabilized. The analyzed results are presented in subsection 3.3.1.

2.4.3 Grids Sensitivity and Model Validation

The grid independence has been carefully examined to ensure the reliability of the numerical simulation results. For this purpose, five different grids were analyzed to observe the solution's evolution, result stability, and grid sensitivity. The grid sets used consisted of 905,060 cells (grid 1); 1,628,877 cells (grid 2); 2,753,589 cells (grid 3); 4,485,553 cells (grid 4); and 6,001,644 cells (grid 5).

In the mesh test simulation, the liquid jet velocity at the nozzle outlet is set at 1.4 m s^{-1}. During its evolution, this velocity decreases until reaching lower speeds for the detachment of the ice, which has already been experimentally determined (see section 3.3). For instance, in the experimental case where the liquid jet velocity is set at 1.4 m s^{-1}, the ice detachment length is 0.116 m at a temperature of −6 °C (see Table 3), and the experimentally found ice non-detachment velocity is 0.51 m s^{-1} (see Figure 22).

The parameter evaluated during the mesh sensitivity test simulations is the jet velocity along the central line at position 0.113 m (see Figure 9, with the nozzle outlet considered as the origin), where the jet velocity reaches values at which detaching the ice layer is no longer possible experimentally at a speed of 0.51 m s^{-1} (see Figure 23 and Table 3). The results of the effect of increasing the number of mesh elements on the solution evolution are presented in Figure 10. It is worth noting that, according to this figure, the results are independent of the grid size for a number of elements greater than 2,753,589 cells.

Considering the simulation's accuracy and computational efficiency, the final number of cells for this study was set to 2,753,589 to reduce the computation time, as using 6,001,644 cells would result in a 24-hour calculation time.

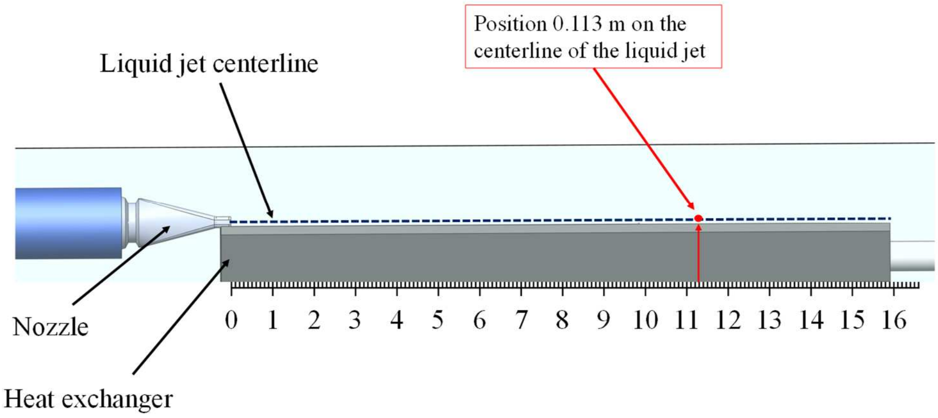

Figure 9 – Spatial representation of the position 0.113 m on the central line of the liquid jet, where the velocity is calculated to test grid independence.

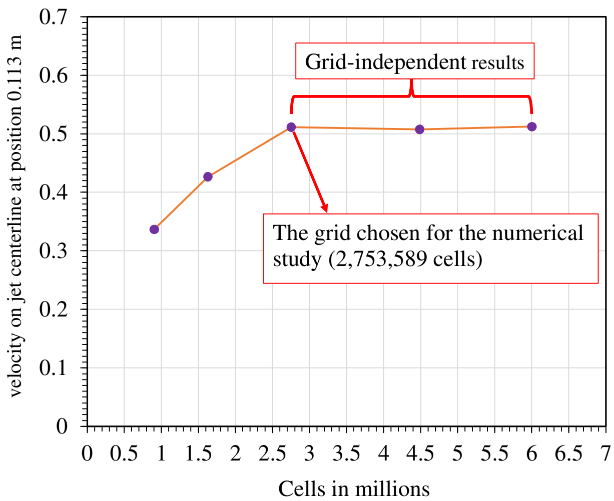

Figure 10 – Evolution of liquid jet velocity result on its central line at the position 0.113 m as a function of the number of grid cells studied.

3. Results and discussions

In this section, the results were analyzed and discussed regarding the effect of temperature, surface conditions (roughness and wetting properties) on the growth, adhesion, and detachment of the ice layer by the flow. The objective is to better understand these phenomena in immersion to determine the optimal conditions for ice slurry production.

3.1 Wettability and surface roughness characterization

Surface wettability is divided into three categories [34,35]:

- hydrophilic surfaces are characterized by a contact angle (*CA*) with a drop of water of less than 90°.
- hydrophobic surfaces are characterized by a contact angle of greater than 90° and less than 150°.
- Superhydrophobic surfaces are characterized by a contact angle of greater than 150° and a contact angle hysteresis *CAH* < 10°.

Three types of AW1050H24 aluminum surfaces (hydrophilic (reference), hydrophobic, and superhydrophobic) were characterized to determine their ability to reduce ice adhesion. The liquid drop volume used for characterization is 8.4 µL of a 10 wt.% ethanol/water mixture, this volume being neither too large to avoid crushing of the drop by gravity effect nor too small to avoid surface tension effects. Measurements are repeated 4 times at an ambient temperature of 23 °C to verify the non-variation of the contact angle, the uncertainty is about ±1°. The first surface is made of untreated (hydrophilic) aluminum and exhibits an average contact angle (average of left and right contact angles) of 58.21°, as shown in Figure 11 (a), while this surface forms an average contact angle of 82.36° with a drop of deionized water [28,29]. The second aluminum surface (same material) which is treated with the 13 µm thick PTFE adhesive tape presents an average contact angle of 91.38°, as shown in Figure 11 (b). The third surface, which is treated with the commercial superhydrophobic coating "Ultra Ever Dry" (UED), exhibits an average contact angle of 151.50°, as shown in Figure 11 (c). This coating was already characterized in a previous study with a deionized water drop of 8.4 µL, with an average contact angle of 157.59° in the Cassie state [28,29].

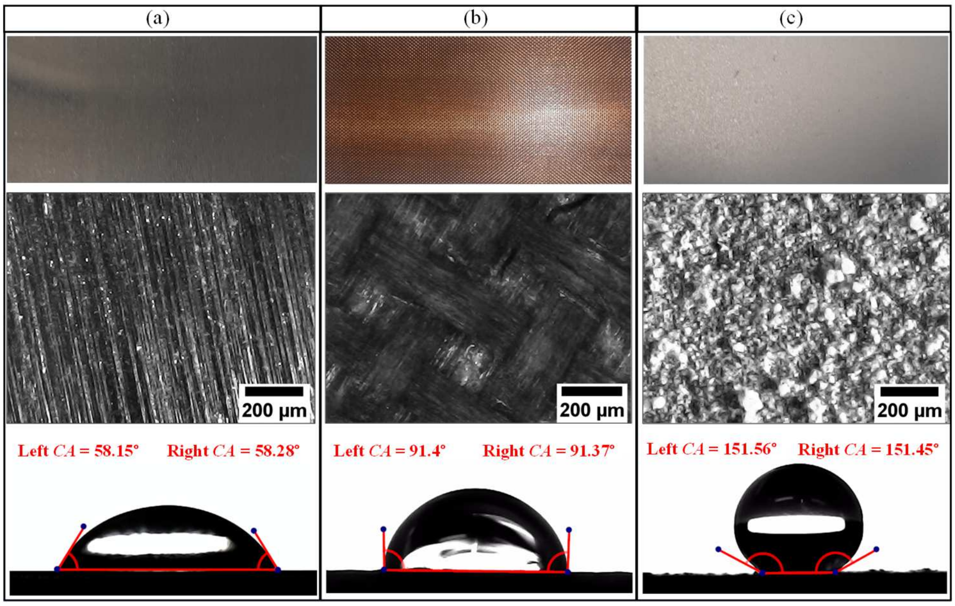

Figure 11 – Microscopic images and contact angles of the three types of surfaces studied, (a) hydrophilic "untreated aluminum"; (b) hydrophobic "aluminum treated with PTFE adhesive tape"; (c) superhydrophobic "aluminum treated with UED coating".

The roughness analysis of the three types of surfaces studied was performed using a KEYENCE VHX-7000N/VHX-970N digital microscope. Figure 12 presents the results of the measurement of the surface roughness parameter *Sa*, which is the arithmetic mean height. This parameter *Sa* extends the *Ra* parameter (arithmetic mean height of a line) to a surface, while the surface roughness *Sz* represents the maximum height. This *Sz* parameter is defined as the sum of the maximum peak height value and the greatest well depth in the defined area. As seen in Figure 12 (a), the untreated aluminum (hydrophilic) surface has the lowest surface roughness (*Sa* = 0.2 µm and *Sz* = 1.3 µm). The aluminum surface treated with PTFE adhesive ribbon (hydrophobic) has a double surface roughness, one at the scale of a single fiber (*Sa* = 2.3 µm and *Sz* = 18.9 µm) and the other at the scale of fibrous tissue surface (*Sa'* = 8.4 µm and *Sz'* = 92.2 µm), as shown in Figure 12 (b). The aluminum surface treated with UED coating (superhydrophobic), as shown in Figure 12 (c), has the highest surface roughness (*Sa* = 12 µm and

Sz = 83.4 µm) compared to the surface roughness of the untreated aluminum and the surface roughness of a single fiber of the PTFE tape.

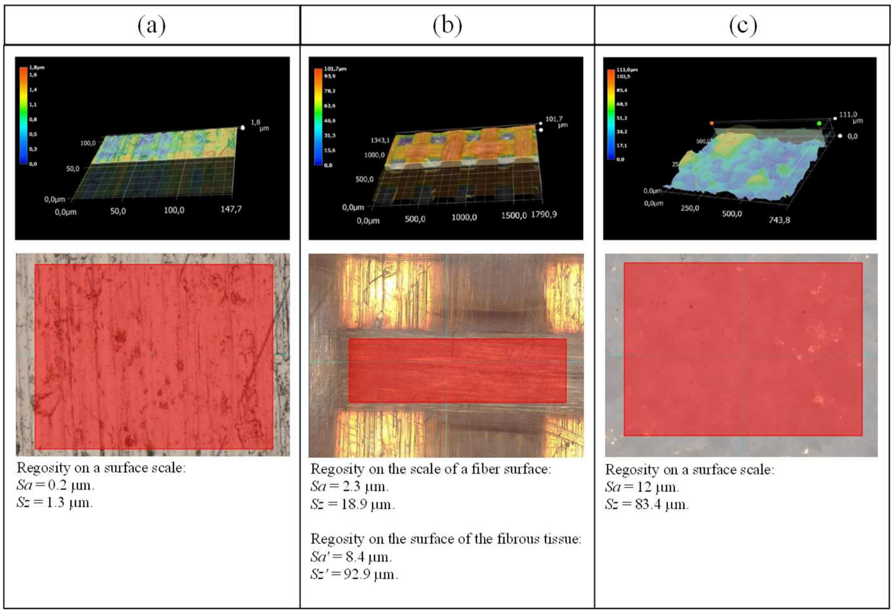

Figure 12 – Results of the measurement of surface roughness parameters "*Sa*" and "*Sz*" of the three types of surfaces studied: (a) hydrophilic; (b) hydrophobic and (c) superhydrophobic.

3.2 Ice growth kinetics

The effect of decreasing surface temperature on ice type and ice growth kinetics on the untreated aluminum surface was examined. In addition, the effects of surface roughness on ice growth kinetics were also analyzed on three types of surfaces: hydrophilic (untreated aluminum), hydrophobic (aluminum treated with PTFE adhesive tape), and superhydrophobic (aluminum treated with UED coating).

3.2.1 Temperature effect on ice growth kinetics

Figure 13 shows the growth kinetics of an ice layer up to 2 mm thick on an untreated aluminum surface (hydrophilic) as a function of time for different surface temperatures set at –6 °C, –8 °C and –9 °C. In addition, Figure 14 shows the evolution of the temperature of the surface and of the 10 wt.% ethanol/water mixture in the surface testing section for different target surface temperatures (–6 °C, –8 °C and –9 °C).

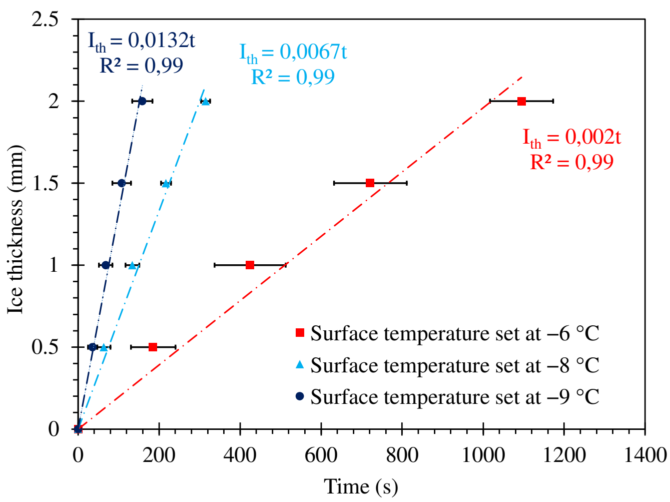

Figure 13 – Growth kinetics of an ice layer up to 2 mm thick on an untreated aluminum surface as a function of time for different surface temperatures set at –6 °C, –8 °C and –9 °C.

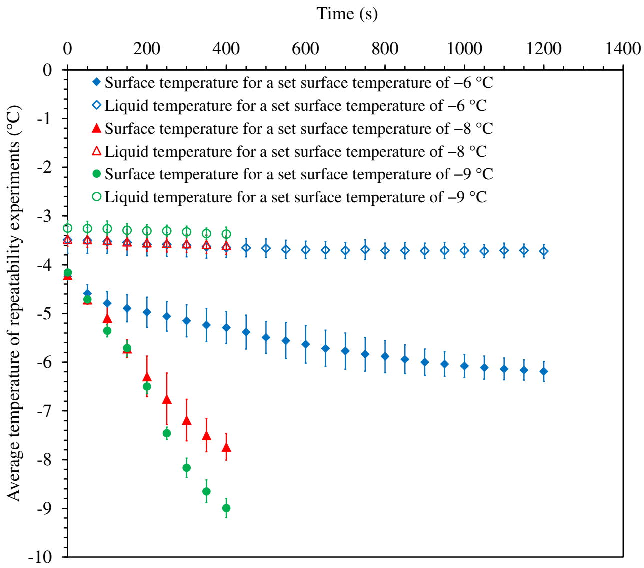

Figure 14 – Evolution of the temperature of the liquid mixture and of the untreated aluminum surfaces during the cooling process for three target surface temperatures of –6 °C, –8 °C and –9 °C.

Figure 13 clearly indicates that a decrease in surface temperature leads to an increase in the ice layer growth rate, as the heat flux increases with the decrease in surface temperature. Furthermore, the standard deviations for the –6 °C case are significant, as shown in Figure 14, because the maximum surface temperature is –6 °C and the average liquid temperature is –3.60 °C. The average temperature between the surface and the liquid gives a value close to the phase change temperature, and in this case, it is difficult to pass the energy barrier necessary for crystallization. Furthermore, the standard deviation of the surface temperature in repeatability experiments is significant. This is due to the formation of an ice layer on the surface, which acts as an insulation and therefore causes variability in the surface temperature.

3.2.2 Effect of surface condition on ice growth kinetics

Figure 15 shows the analysis of the temperature evolution of the three surfaces: hydrophilic (untreated aluminum) as "Al", hydrophobic (aluminum treated with Teflon® coating) as "PTFE", and superhydrophobic (aluminum treated with Ultra Ever Dry) as "UED", and the temperature of the 10 wt.% water-ethanol mixture as a function of time during the surface cooling process. These temperatures are plotted for a surface temperature between –4.10 °C and a final temperature of –8 °C, between which a layer of ice with a maximum thickness of 2 mm is generated. It is observed that the temperature variation of the ethanol/water mixture is stable for the three surfaces (Al, PTFE and UED), with a standard deviation of less than ±0.25 °C. Concerning the surface temperature the standard deviation does not exceed ±0.6 °C.

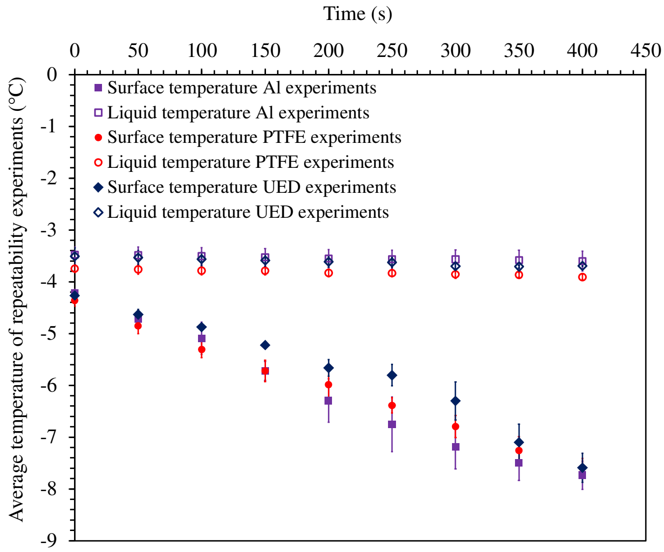

Figure 15 – Evolution of the temperature of the liquid mixture and the three types of surfaces studied during the surface cooling process.

Figure 16 shows the ice growth kinetics as a function of time for the three types of surfaces and for a target surface temperature of –8 °C. The results indicate that ice growth is faster on the superhydrophobic UED surface when compared to the PTFE and Al surfaces, even though the surface temperature of the UED surface is slightly warmer than the others. Additionally, ice growth is slower on the Al surface when compared to the PTFE surface. The aluminum surface treated with the UED superhydrophobic coating increases the crystallization rate due to its higher roughness (Sa = 12 µm, as described in section 3.1). This value is significantly higher than PTFE (Sa = 2.3 µm *and* Sa' = 8.4 µm) and untreated aluminum (Sa = 0.2 µm), providing more nucleation sites on this superhydrophobic UED surface. Indeed, roughness contributes to lowering the energy barrier for crystallization, as already demonstrated in the article by Cao et al. [36]. The authors studied various superhydrophobic coatings based on nanoparticle-polymer composites with diameters D_p = 20 nm, 50 nm, 100 nm, 1 µm, and 20 µm, with contact angles ranging from 143° to 158°, and a contact angle hysteresis of 2° and 4°. The authors analyzed the effect of nanoparticle size in the superhydrophobic coating on the free energy barrier. They noticed that the energy barrier for nucleation continuously decreases with an increase in the size of particles in the superhydrophobic coating (increase in roughness) [36].

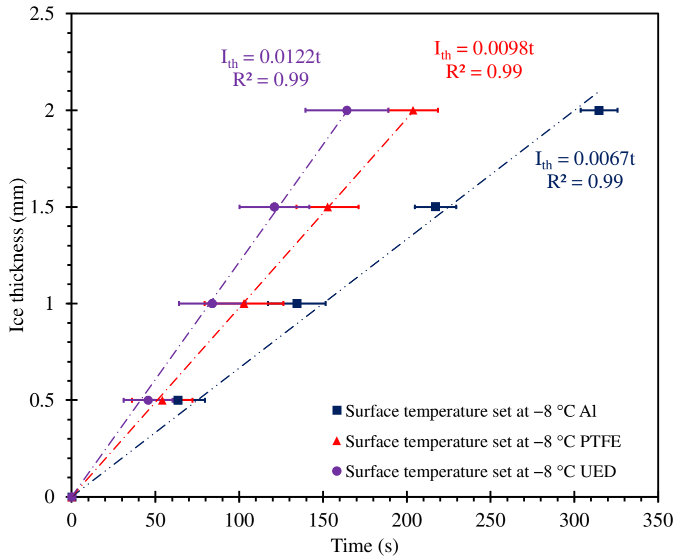

Figure 16 – Ice growth kinetics as a function of time for a target surface temperature of –8 °C on the three surface types.

However, the PTFE surface has a double roughness due to its texture (glass fiber) of *Sa'* about 8.4 µm and a roughness on the fiber surface (*Sa* = 2.3 µm). This double roughness also serves as a nucleation site, explaining why crystallization is faster on the PTFE surface compared to the untreated aluminum surface, which is characterized by a roughness of *Sa* = 0.2 µm. The surface roughness plays an important role in influencing the crystallization rate of the ice by providing increasing the surface area available for crystallization. This leads to a higher crystallization rate due to the increased number of nucleation sites available for crystals.

The behavior of submerged superhydrophobic surfaces is aerophilic, meaning that they trap air in their roughness when submerged [37]. Initially, the immersed UED superhydrophobic surface is covered with a thin layer of air visible as a silvery mirror-like reflection, which is the signature of the presence of an air layer adhering to the surface. During the cooling process, the silvery mirror reflection becomes clearer and less reflective (seen by the naked eye), and then disappears when reaching low negative temperatures (–6 °C). These experiments aim to understand the wetting behavior of the UED superhydrophobic surface under immersion with surface cooling and understand why the silver mirror color reflectivity effect that disappears during surface cooling. Figure 17 shows the air bubbles placed with a pipette on the UED superhydrophobic surface in immersion to verify and understand the physical phenomena of wetting transition in immersion with surface cooling.

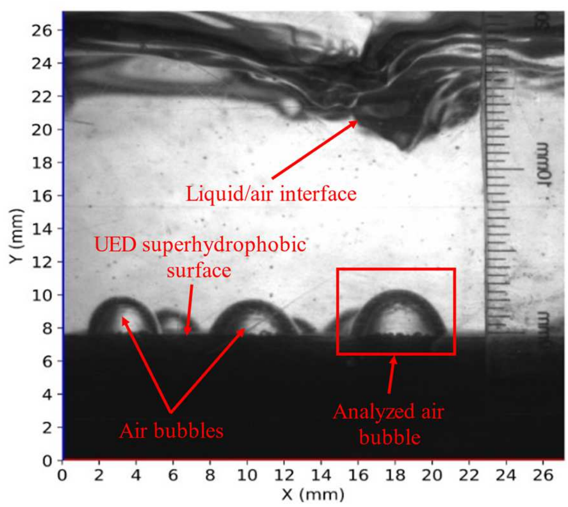

Figure 17 – Air bubbles deposited on the superhydrophobic UED surface immersed in a 10 wt.% ethanol/water mixture during the cooling process, the surface temperature T_s is 3.97 °C which corresponds to time t = 1622 s.

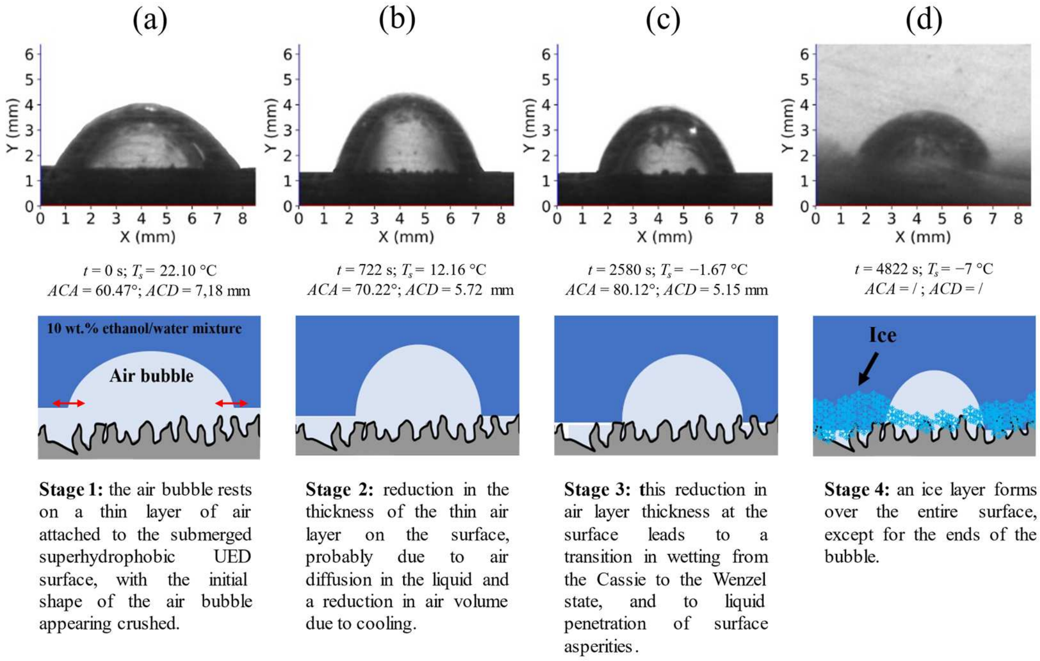

Figure 18 – Real image of the air bubble without background and schematic model illustrating the wetting transition on a UED superhydrophobic surface immersed in a 10 wt.% ethanol/water mixture during the surface cooling process. T_s is the surface temperature, *ACA* represents the air bubble contact angle, and *ACD* represents the air bubble contact diameter.

Figure 18 shows the real images and a schematic model explaining the behavior of air bubbles and the wetting transition when immersed in a 10 wt.% ethanol/water mixture on a cooled superhydrophobic UED surface. This model is considered original because no previous study has verified this wetting behavior in immersion and at low temperature. When the air bubble is deposited at a temperature of 22.10 °C on the immersed superhydrophobic UED surface, as shown in Figure 18 (a), the initial shape of the air bubble appears to be squashed. This air bubble has an *ACA* air contact angle of 60.47° and an *ACD* air contact diameter (air bubble base diameter) of 7.18 mm. At this temperature of 22.10°, the air bubble slides from left to right across the surface due to its contact with the thin layer of air and the agitation of the mixture caused by the flow. As the surface temperature decreases, the silvery mirror color becomes less visible, indicating a reduction in the thickness of the thin layer of air on the surface, likely due to air diffusion into the liquid and a decrease in air volume due to cooling. This decrease in the thickness of the air layer on the surface leads to a decrease in the contact diameter of the air bubble (*ACD* = 5.72 mm) and an increase in its contact angle (*ACA* = 70.22°) due to buoyancy forces lifting the bubble vertically, as shown in Figure 18 (b). In the end, a layer of ice forms over the entire surface, except for the ends of the bubbles which remain in contact with the cooled superhydrophobic surface due to the lack of contact between the liquid and this cooled surface, as shown in Figure 18 (d). Figure 19 shows the process of ice layer formation on the surface of the UED in the presence of air bubbles. After the transition from the Cassie wetting state to the Wenzel state, ice forms across the entire surface except at the locations of air bubbles in immersion, which isolate the liquid from the cold UED surface.

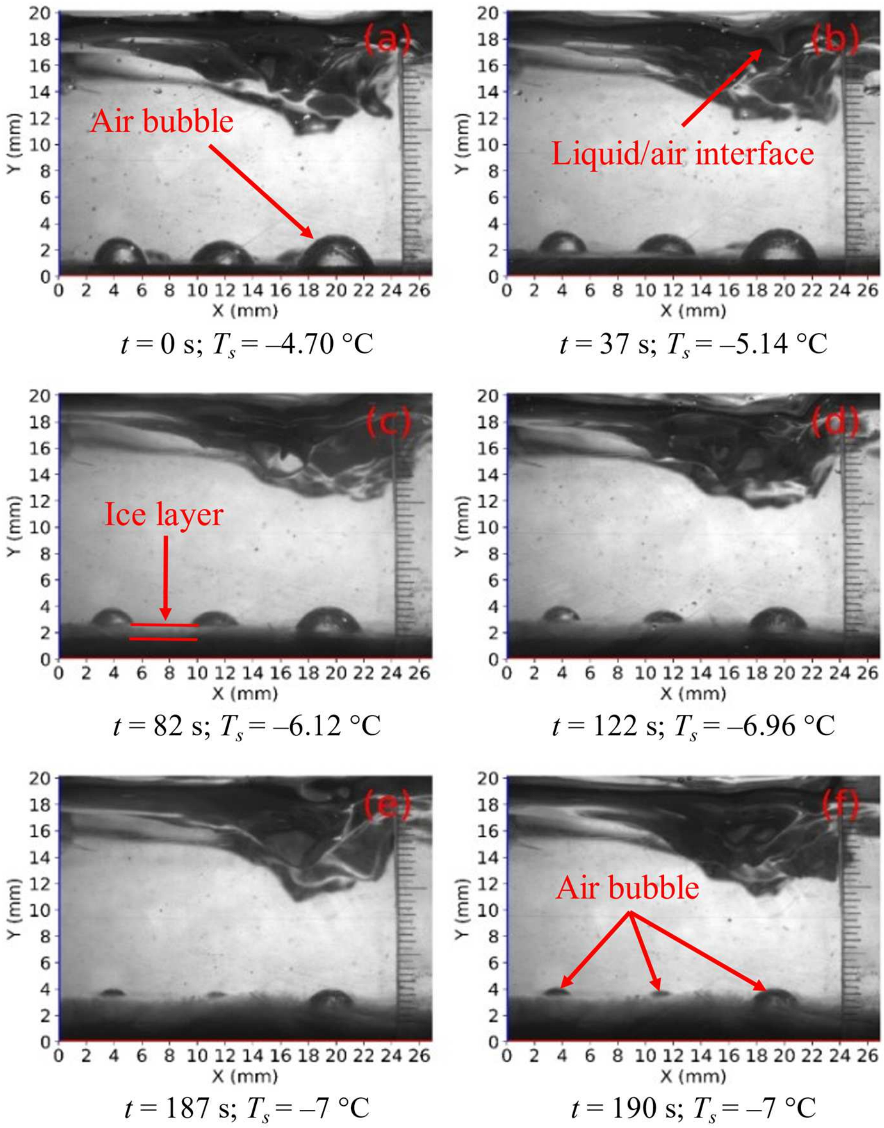

Figure 19 – Formation of a 2 mm ice layer on the UED superhydrophobic surface in a 10 wt.% ethanol/water mixture.

3.3 Ice detachment length evolution

In this subsection, the evolution of L_D on the three types of surfaces: hydrophilic (untreated aluminum), hydrophobic (aluminum treated with PTFE adhesive tape), and superhydrophobic (aluminum treated with a UED superhydrophobic coating) was studied.

3.3.1 Temperature effect on ice detachment length

The experimental results presented in Figure 20 show the detachment of a 2 mm thick ice layer on an untreated aluminum surface. The surface temperature was set at –6 °C, and the liquid velocity at the nozzle outlet (V_N), which was oriented horizontally towards the surface, was 1.62 m s^{-1}. The detachment process lasted about 1.27 s, and the type of detachment was identified as adhesive, meaning the ice detached from the surface without leaving any residue. The ice was characterized as soft, with needle-like crystals due to the presence of ethanol. After detachment, the ice broke into small particles, as shown in the images in Figure 20 (c) and 20 (e). Chemical additives have an effect on the morphology of the ice; for example, seawater (brine) results in porous ice [14,20–22,38]. These additives change the nature of the ice, making it soft, and the ice crystals often take on the shape of needles, reducing the contact surface of the ice with the solid surface. If pure water is used to produce the ice, it will have a hard texture [22,28]. In the case of a surface temperature set at –8 °C, ice detachment and ice appearance are similar to those observed at a surface temperature of –6 °C.

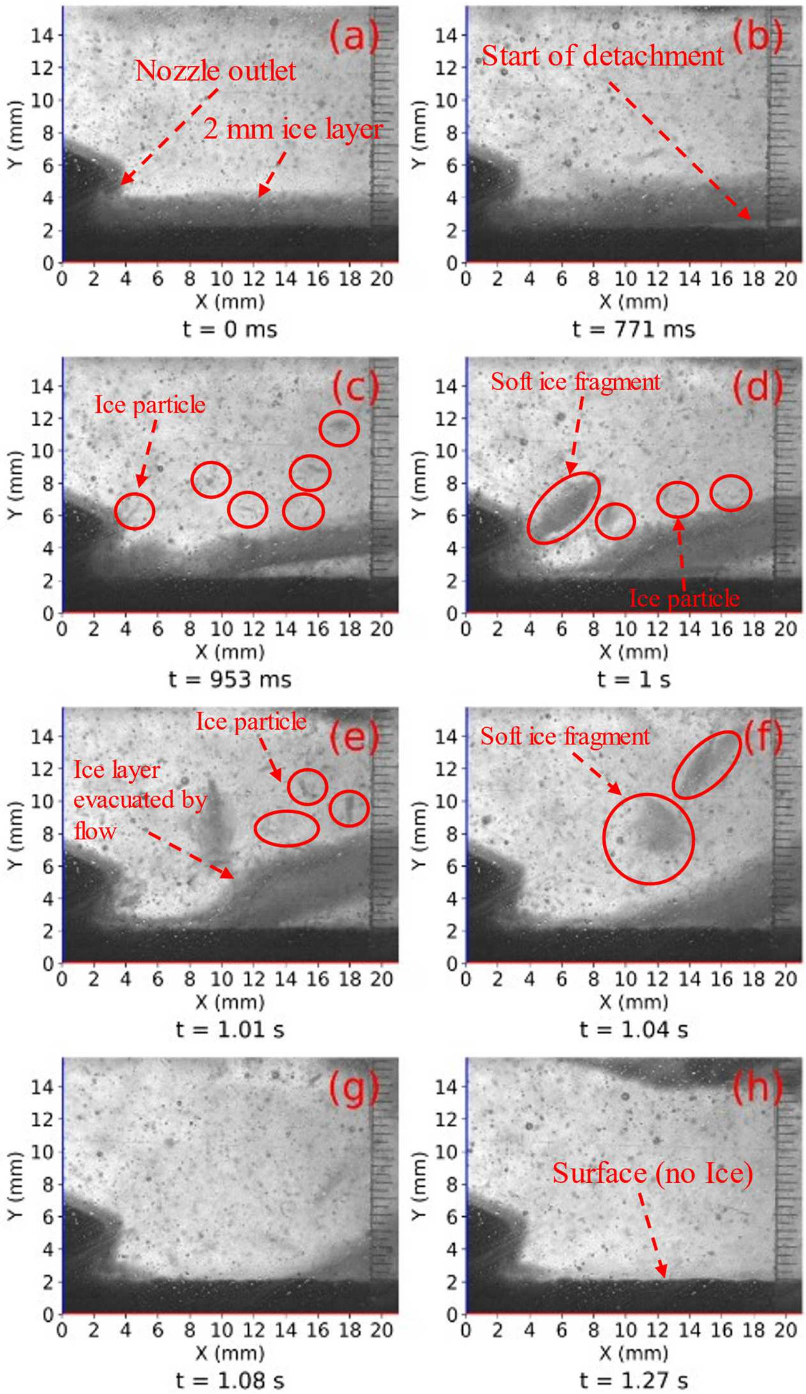

Figure 20 – Image of ice layer detachment on an untreated aluminum surface for a surface temperature set at –6 °C and an average velocity at the nozzle outlet V_N of 1.62 m s^{-1}.

Figure 21 shows the results of detaching a 2 mm thick ice layer from an untreated aluminum surface at a surface temperature set at –9 °C. The average liquid velocity at the nozzle outlet is 1.62 m s^{-1}, which is identical to the –6 °C case described earlier. The ice detachment process took approximately 1.74 s, slightly longer than in the –6 °C case. As with the –6 °C case, the type of detachment observed was adhesive, where the ice layer fully detached from the surface without leaving any residue, as depicted in Figures 21 (c)-(f). However, the ice layer does not detach easily, and the ice is hard, in contrast to the soft ice observed at –6 °C. The detachment of the ice layer at a temperature of –9 °C occurred in large hard fragments rather than small particles, as shown in Figure 21 (f). This ice hardening is due to the effect of low temperature, which accelerates the crystallization process, leading to a densification of the ice layer. This effect of temperature has already been observed in a previous study with a 10 wt.% aqueous urea solution [22].

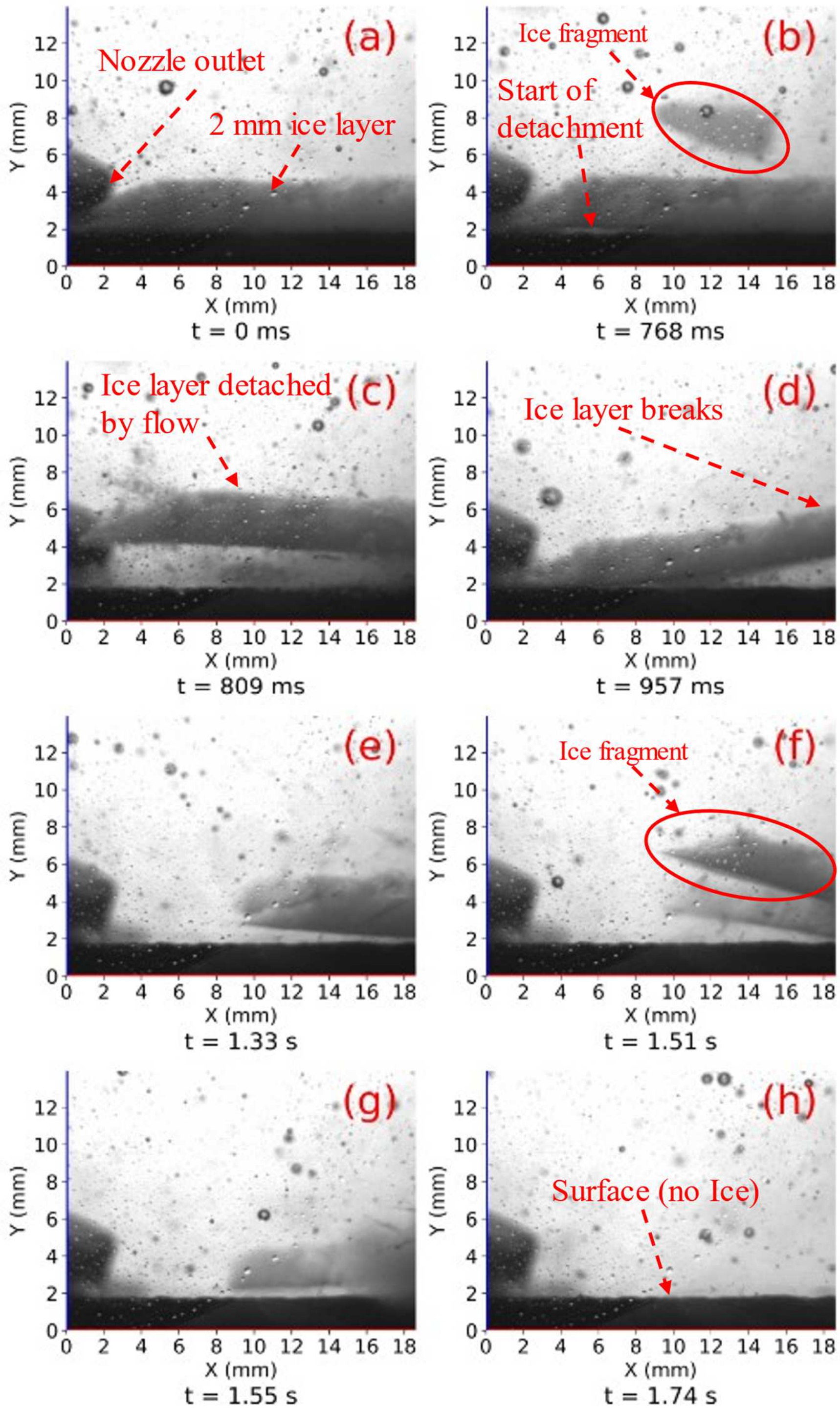

Figure 21 – Image of ice layer detachment on an untreated aluminum surface for a surface temperature set at –9 °C and an average velocity at the nozzle outlet of 1.62 m s^{-1}.

Figure 22 shows the variation of the ice detachment length L_D as a function of the average liquid velocity at the nozzle outlet along a 0.16 m long surface. In our experiments, the mass flow rate ranges from 0 to 0.17 kg s^{-1}. This implies a flow velocity at the nozzle outlet ranging from 0 to 2.87 m s^{-1}. The experiments were conducted on an untreated aluminum surface (hydrophilic) at three different surface temperatures (–6 °C, –8 °C and –9 °C). In our experiments, we calculated the flow velocity V_N at the nozzle outlet using the following equation (Eq. 2):

$$V_N = \frac{Q_m}{\rho_l S_N} \qquad \text{Eq. (2)}$$

Where Q_m is the mass flow rate, ρ_l is the density of the mixture, and S_N is the outlet cross-sectional area of the nozzle. As shown in Figure 22, the limit velocity of ice non-detachment V_{IND}, i.e., the velocity below which there is no detachment of ice from the surface, is 0.51 m s^{-1}, 0.64 m s^{-1}, and 1.08 m s^{-1} for surface temperatures set at –6 °C, –8 °C, and –9 °C, respectively. The ice detachment length decreases with decreasing surface temperature due to an increase in ice adhesion strength, which is a well-known trend in the literature [14,22,39]. At –6 °C and –8 °C, the required velocity V_N to detach the ice over the entire surface is 2.45 m s^{-1} and 2.87 m s^{-1}, respectively. However, for the –9 °C surface temperature case, the detachment length is limited to 0.133 m, and the maximum velocity V_N in our experiments does not exceed 2.87 m s^{-1}, which prevents us from detaching ice along the entire surface length. The standard deviations on the –9 °C curve are larger due to the production of a hard ice layer (see Figure 21) compared to the soft ice layer produced at surface temperatures of –6 °C and –8 °C (as shown in Figure 20), resulting in the detachment of large hard fragments from the surface and leading to the variability of the detachment length over the three repeatability experiments. An analysis of error propagation for measurements of various parameters, such as liquid jet velocities and ice detachment lengths (L_D), has been conducted. The absolute uncertainties are estimated using the Student's distribution with a 95% confidence interval [40]. The measurement errors for liquid jet velocities and ice detachment lengths (LD) in Figure 22 are presented in Tables A1, A2, and A3 of Appendix A.

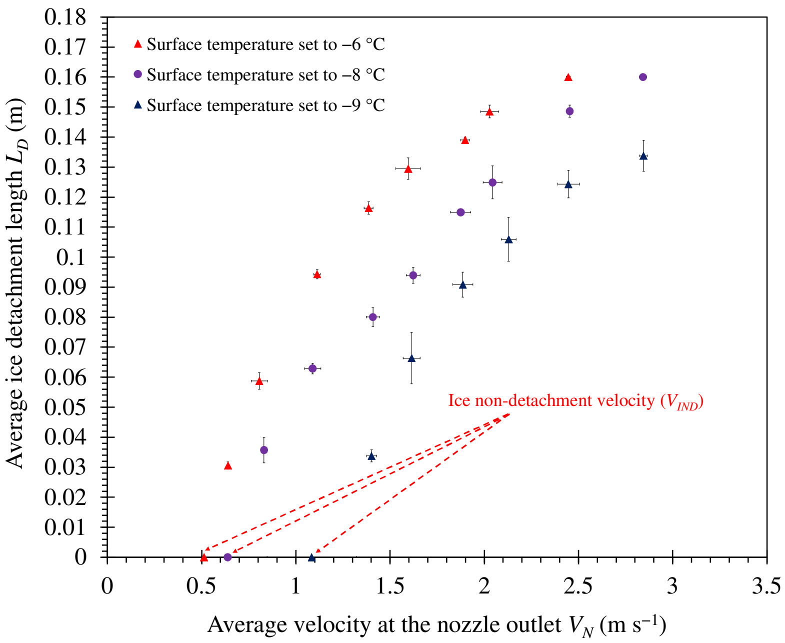

Figure 22 – Evolution of the ice detachment length L_D as a function of the average velocity at the nozzle outlet for an untreated aluminum surface, for the three surface temperatures set at –6 °C, –8 °C and –9 °C.

3.3.1.1 Numerical and experimental comparison on the ice detachment length

Figure 23 shows the results of ANSYS® Fluent numerical simulations using the numerical method described in subsection 2.4. It shows the evolution of the local velocity of the turbulent jet (for flow velocities at the nozzle outlet V_N from 1.4 m s^{-1} to 2.87 m s^{-1}) from the nozzle outlet which is at the 0 m position to the 0.16 m position of the untreated aluminum surface (along the nozzle centerline). The dashed lines represent the limit velocity of ice non-detachment V_{IND}, determined previously from the velocity at the nozzle outlet (see Figure 22), for the cases of surface temperatures set at –6 °C, –8 °C, and –9 °C, which are 0.51 m s^{-1}, 0.64 m s^{-1}, and 1.08 m s^{-1}, respectively. The purpose of this numerical model is to determine the maximum length, L_{Max}, for which the local velocity of the liquid jet reaches the limit velocity of ice non-detachment V_{IND}, and compare it with the experimentally ice detachment length determined previously, L_D. According to Figure 23, the local velocity of the jet increases after passing through the nozzle outlet due to the decrease in jet pressure, resulting in a slight increase in velocity. This velocity then decreases along the jet axis (along the surface). Near the 0.16 m position, there is an increase in velocity due to the discharge outlet (as seen in component 6 of Figure 3), which causes a flow acceleration.

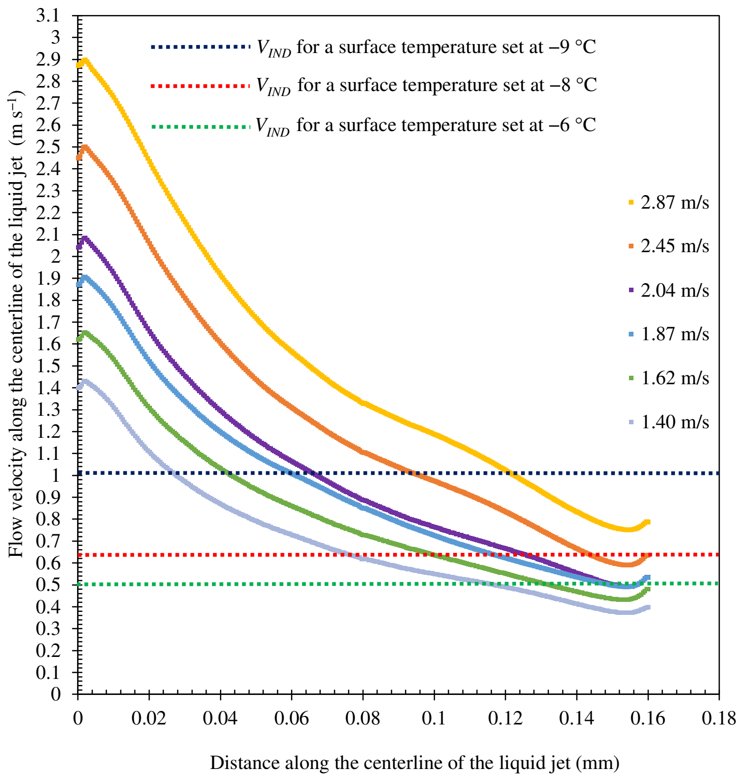

Figure 23 – Evolution of the numerical turbulent velocities of the liquid jet along its centerline for an untreated aluminum surface and for the three surface temperatures fixed at –6 °C, –8 °C and –9 °C.

Table 3 presents a comparison of the numerical results obtained with ANSYS® Fluent, which show the maximum length, L_{Max}, for which the local velocity of the liquid jet reaches the limit velocity of ice non-detachment (V_{IND}), and the experimental ice detachment length, L_D, for the three surface temperatures set at –6 °C, –8 °C, and –9 °C.

Table 3 – Comparison between the maximum numerical length L_{Max} for which the local velocity of the liquid jet reaches the limit velocity of ice non-detachment (V_{IND}), and the experimental ice detachment length L_D at different surface temperatures set at –6 °C, –8 °C and –9 °C.

Velocity at nozzle outlet V_N (m s^{-1})	**Reynolds (/)**	**Surface temperature –6 °C**		**Surface temperature –8 °C**		**Surface temperature –9 °C**	
		L_{Max} NUM (m)	**L_D EXP (m)**	**L_{Max} NUM (m)**	**L_D EXP (m)**	**L_{Max} NUM (m)**	**L_D EXP (m)**
2.87	5545	0.16	0.16	0.16	0.16	0.114	0.133
2.45	4783	0.16	0.16	0.144	0.148	0.083	0.124
2.04	3983	0.146	0.148	0.126	0.124	0.058	0.105
1.87	3651	0.144	0.139	0.117	0.114	0.05	0.09
1.62	3163	0.128	0.129	0.100	0.093	0.035	0.066
1.40	2733	0.113	0.116	0.077	0.080	0.021	0.033

It can be seen in Table 3 that the relative differences between the L_{Max} lengths of the numerical simulations (NUM) and the L_D lengths of the experimental results (EXP) for the case of surface temperatures set at –6 °C and –8 °C, are not significant, i.e. with a maximum difference (relative deviation) less than 8%, which indicates the validation of our numerical model for the case of these two surface temperatures. Indeed, the positions found numerically for which the local velocity of the liquid jet reaches the ice non-detachment velocity (V_{IND}) are very close to the ice detachment positions found experimentally. This can be explained by the fact that in these two cases of surface temperature fixed at –6 °C and –8 °C, the ice produced and detached is soft and the detachment stops at the position where the liquid jet velocity reaches the ice non-detachment velocity. However, for the case of the surface temperature fixed at –9 °C (see Table 3), the relative deviations are very large, above 8%. In this case the numerical model is not able to predict the position of the ice non-detachment velocities because in this case the ice detaches in large hard fragments in a less repeated way, which results in a very high relative deviation. Therefore, our numerical model is only valid in the case where the detached ice is soft for the –6 °C and –8 °C surface temperature cases.

3.3.1.2 Evaluation of liquid jet force on ice detachment

In this part, an evaluation of the liquid jet force is presented along with an empirical model to estimate the effect of this force on the evolution of the ice detachment length L_D on the untreated aluminum surface for the three surface temperatures set at –6 °C, –8 °C, and –9 °C. The force of the jet at the nozzle outlet F_N can be calculated using the following equation (Eq.3):

$$F_N = Q_m V_N = \rho_l S_N V_N^2 = 2P_D S_N \quad \text{Eq. (3)}$$

Where ρ_l is the density of the fluid, Q_m is the mass flow rate at nozzle outlet, S_N is the nozzle outlet cross-section, $P_D = 0.5\rho_l V_N^2$ is the dynamic pressure at the nozzle outlet, and V_N is the flow velocity at the nozzle outlet.

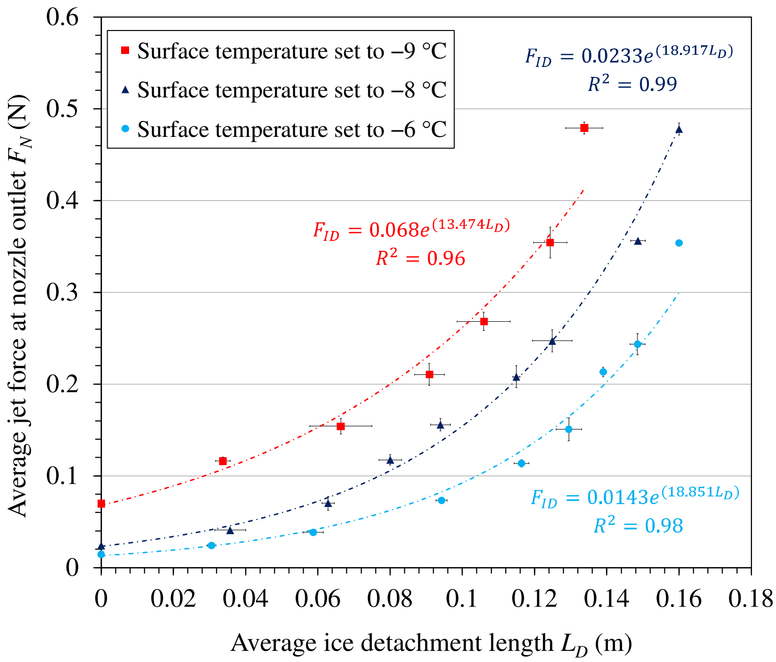

Figure 24 – Evolution of the jet force at the nozzle outlet for ice detachment F_{ID} as a function of the ice detachment length L_D for an untreated aluminum surface and this for the three cases of surface temperature fixed at –6 °C, –8 °C and –9 °C.

Figure 24 shows the liquid jet force at the nozzle outlet as a function of the ice detachment length obtained with equation (Eq.3) for the case of the untreated aluminum surface with surface temperature variation. It can be observed that the force of the liquid jet at the nozzle outlet for ice detachment F_{ID} (Force Ice Detachment) varies with the ice detachment length and has an exponential curve. Using this curve, a force model of the form shown in Equation (Eq.4) is obtained:

$$F_{ID} = F_0 \exp(kL_D) \qquad \text{Eq. (4)}$$

Where F_0 represents the force below which there is no ice detachment, L_D the ice detachment length which varies between 0 and 0.16 m, and k a constant that depends on several experimental parameters such as surface temperature, immersion level, jet force dissipation, and configuration geometry. This model provides minimum force F_0 values required for ice detachment, as well as maximum values F_{Max} for full surface ice detachment, for each temperature, as shown in Table 4:

Table 4 – Minimum, maximum force for ice detachment for each investigated surface temperature.

Temperature (°C)	Minimum forces F_0 (N)	Minimum velocities V_0 (V_{IND}) (m s^{-1})	Maximum forces F_{Max} (N)	Maximum velocities V_{Max} (m s^{-1})	L_D EXP (m)
– 6	0.014	0.51	0.35	2.44	0.16
– 8	0.023	0.64	0.48	2.84	0.16
– 9	0.068	1.08	0.48	2.84	0.133

Table 4 shows that the force required to detach the ice from the entire surface of the untreated aluminum samples is 0.35 N, when the surface temperature is set at - 6 °C, and 0.48 N when the surface temperature is set at –8 °C and –9 °C. This low force is due to the porosity of the ice layer which reduces the adhesion of the ice to the surface, which may be caused by the presence of ethanol in the aqueous mixture.

As the surface temperature decreases, the force required to detach the ice increases, due to the hardness of the ice and its strong adhesion. It is difficult to compare these experimental forces with literature results [41–43]. Several factors, such as the presence of microcracks, roughness, quasi-liquid micro-layers, etc., affect the adhesion of ice to the surface [14]. Furthermore, this study focuses on the adhesion of ice produced with a water-ethanol mixture, which reduces the adhesion force of the ice to the surface. Indeed, the nature of ice differs from that of pure water. The presence of ethanol makes the ice softer and more porous, even causing the formation of needle-shaped crystals, which reduces its contact with the surface and, consequently, its adhesion. A critical review of the development of a common standard for ice adhesion and different methods of measuring ice adhesion forces was published by Rønneberg et al. [39]. The authors suggest that the measured adhesion forces are very sensitive to both the measurement method and the ice type.

3.3.2 *Surface condition effect on ice detachment length*

In Figure 25, the experimental results are presented for comparing the evolution of the detachment length of the 2 mm thick ice layer (L_D) as a function of the average velocity at the nozzle outlet V_N for a surface temperature fixed at –8 °C. The results are presented for all three surface samples. Error propagation analysis was performed to assess absolute uncertainties, using Student's distribution with a 95% confidence interval [40]. The resulting measurement errors for liquid jet velocities and ice detachment lengths (L_D), shown in Figure 25, are documented in Tables B1 and B2 in Appendix B.

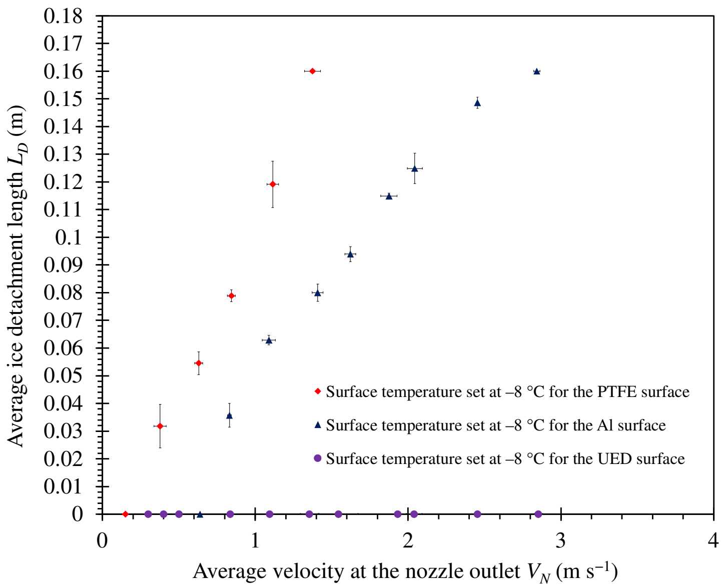

Figure 25 – Evolution of the ice detachment length L_D as a function of the average velocity of the aqueous mixture at the nozzle outlet V_N for three types of investigated samples: untreated aluminum "Al" (hydrophilic), aluminum treated with a Teflon® tape "PTFE" (hydrophobic), and aluminum treated with the Ultra Ever Dry coating "UED" (superhydrophobic).

In Figure 25, it can be observed that there is no visible ice layer detachment on the aluminum surface treated with the UED superhydrophobic coating, as shown in Figure 28, for all flow velocities studied. This result is consistent with the data published in the literature, which indicates that superhydrophobic surfaces do not reduce ice adhesion [41,44]. This is due to the transition from the Cassie state to the Wenzel state, resulting in mechanical interlocking, as demonstrated by Chen et al. [41]. The explanation for this result is the effect of the high roughness of the UED superhydrophobic surface, which is characterized by the roughness parameter S_Z of 83.4 µm, as described in subsection 3.1. This value is significantly higher than that of PTFE (18.9 µm) and untreated aluminum (1.3 µm). The increase in surface roughness leads to an increase in the contact area and the number of potential anchor sites for the ice layer [45]. Four mechanisms can explain the phenomenon of ice adhesion to a surface, as described in a review article published by Samah et al. [14]: the mechanical mechanism, the chemical mechanism, the electrostatic mechanism, and the boundary layer mechanism [46–48]. For the case of the untreated (hydrophilic) aluminum surface, it is noted that there is no visible ice detachment on the surface below a velocity V_{IND} of 0.64 m s^{-1}. To detach all the ice along the 160 mm (0.16 m) exchanger, a velocity V_N of 2.87 m s^{-1} is required. On the aluminum surface treated with PTFE adhesive ribbon, the limit velocity of ice non-detachment V_{IND} is equal to 0.15 m s^{-1}, which is four times less than the limit velocity of ice non-detachment V_{IND} on the untreated aluminum surface. To detach all the ice along the heat exchanger, a velocity V_N of about 1.37 m s^{-1} is required (see Figure 26 (d)), which is half that of the untreated aluminum surface, although the roughness parameter S_Z of PTFE, which is 18.9 µm, is much higher than that of the untreated aluminum surface, which is about 1.3 µm. This result indicates that Teflon® (PTFE) exhibits good ice-repellent characteristics (low ice adhesion) compared to the untreated aluminum surface (hydrophilic) and the UED treated aluminum surface (superhydrophobic). This result is consistent with the results of Brooks et al. [20,21], and the results of ice adhesion tests on Teflon® (PTFE) by Fillion et al. [49]. PTFE is currently one of the best icephobic materials reducing ice adhesion forces due to its low dielectric permittivity of about ≈ 2.1 [50]. In conclusion, the use of a Teflon® (PTFE) coating or tape for ice slurry generation will reduce the amount of energy required to detach the ice from the surface, provided that the Teflon® coating or tape is thin enough to not penalize heat transfer.

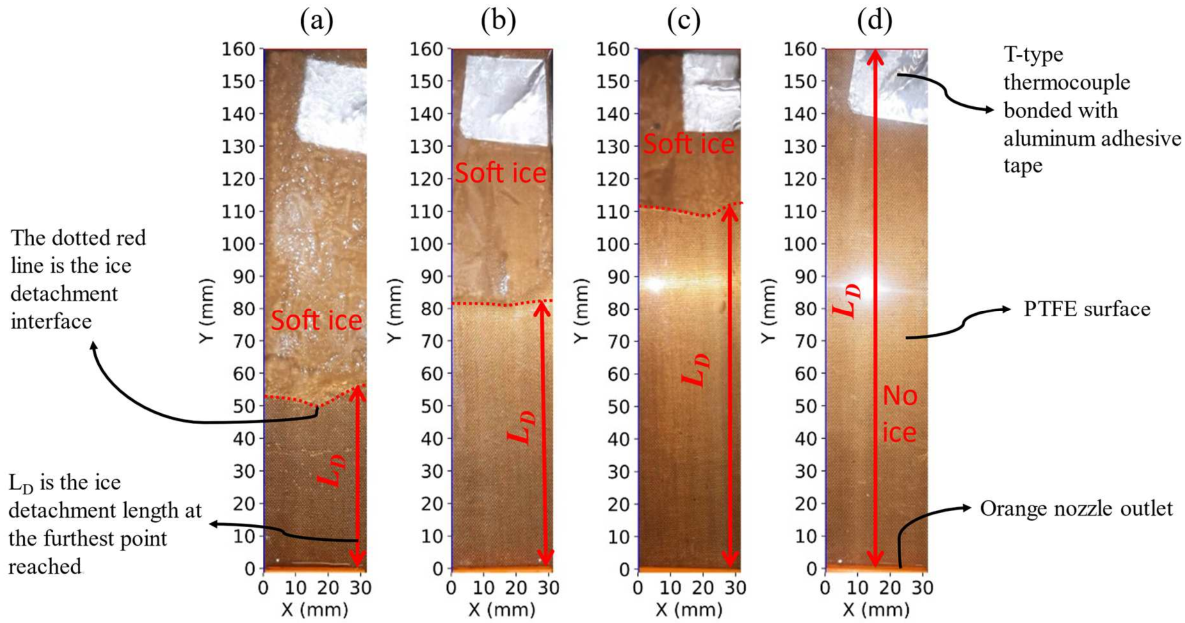

Figure 26 – Example of 4 experiments of the measurement of the ice detachment length "L_D" (m) for the case of an aluminum surface treated with the PTEF adhesive ribbon for a surface temperature fixed at – 8 °C: (a) V_N = 0.64 m s^{-1} and L_D = 0.057 m; (b) V_N = 0.86 m s^{-1} and L_D = 0.083 m; (c) V_N = 1.08 m s^{-1} and L_D = 0.113 m; (d)V_N = 1.41 m s^{-1} and L_D = 0.16 m.

In order to illustrate the icephobic behavior of Teflon® (PTFE), Figure 26 presents the evolution of the ice detachment length (L_D) on the aluminum surface treated with Teflon® (PTFE) ribbon for different flow velocities and a fixed surface temperature of –8 °C. The measurement of the ice detachment length is taken at the point of maximum detachment. It can be seen in this figure that the area where the ice is detached has no ice residue (see also Figure 27), which is consistent with adhesive detachment. The detached ice is soft (needle-like crystals), allowing it to disintegrate into large fragments into particles under the effect of the flow agitation.

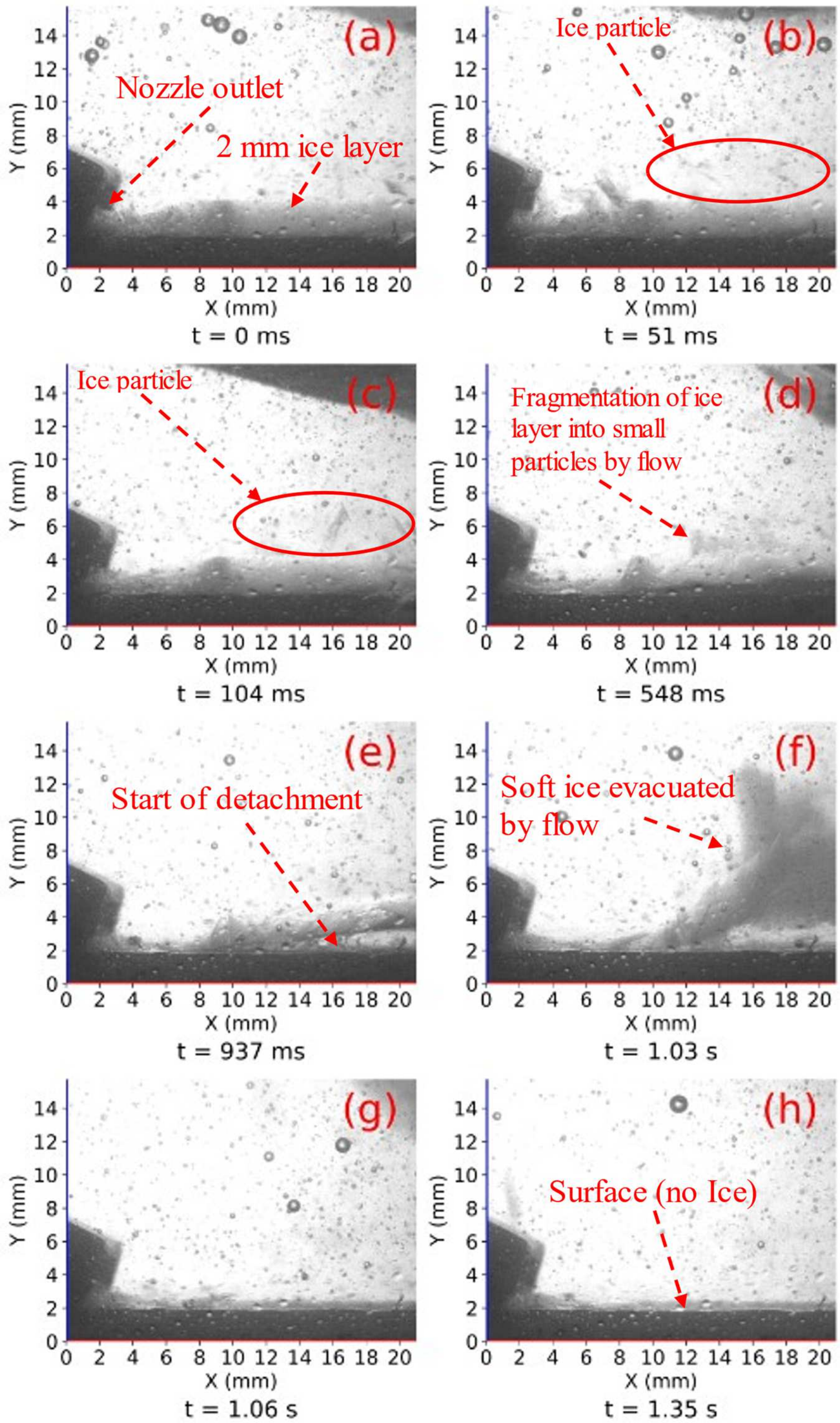

Figure 27 – Image of the ice layer detachment on an aluminum surface treated with PTFE ribbon for a set surface temperature of –8 °C and an average nozzle exit velocity of 2 m s^{-1}.

The high-speed camera images in Figures 27 and 28 show the ice layer detachment on the aluminum surface treated with PTFE adhesive tape and on the aluminum surface treated with Ultra Ever Dry "UED" coating, respectively, for a flow velocity of 2 m s^{-1}.

As shown in Figure 27, the detachment of the ice from the PTFE surface is adhesive, i.e., the entire ice layer detaches from the surface without leaving any ice residue. This ice layer is soft, so it disintegrates into ice particles under the agitation of the flow. After 1.35 seconds, the entire ice layer detaches from the PTFE surface. The ice detaches in the same way on the untreated aluminum surface with adhesive detachment.

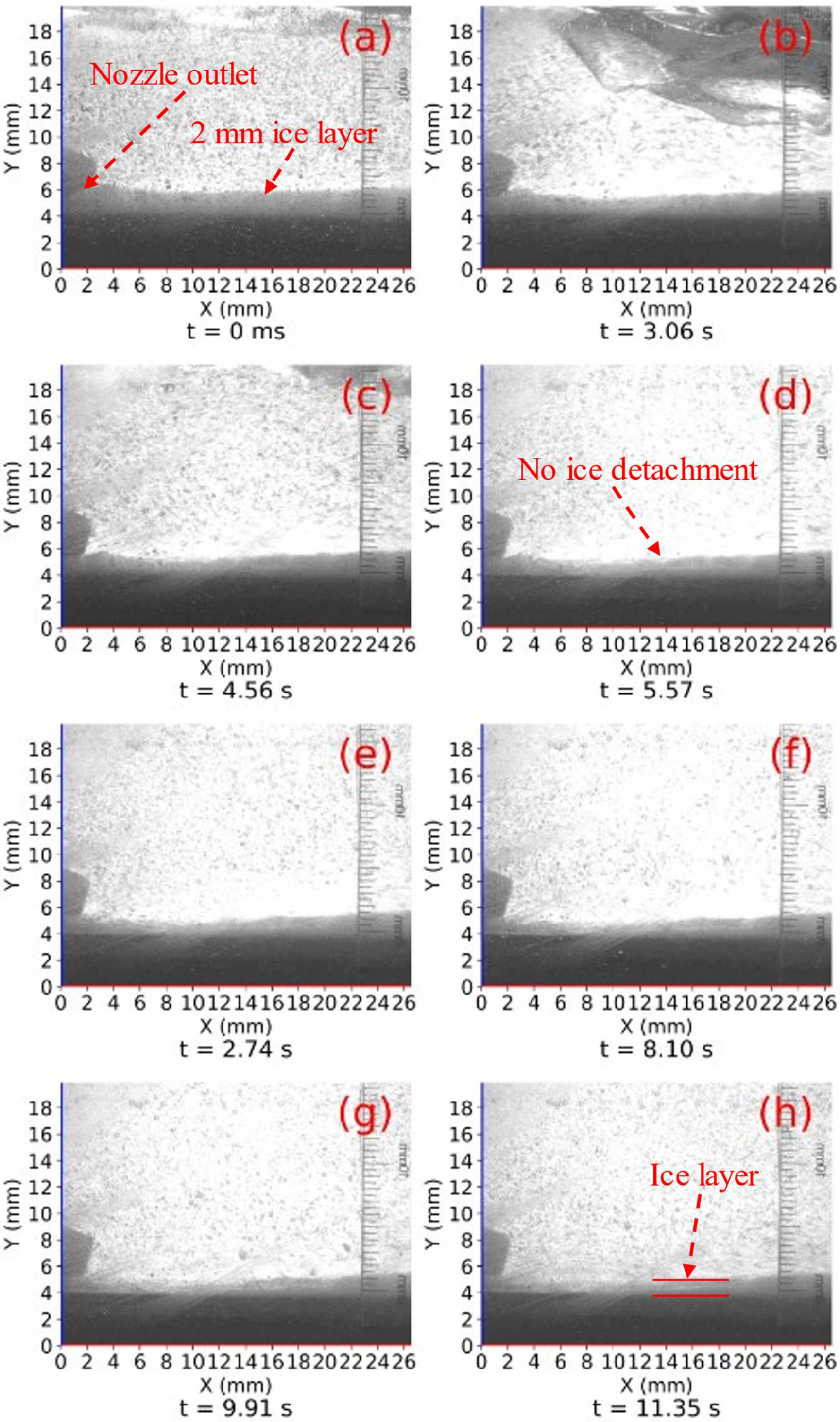

Figure 28 – Image of the ice layer detachment on an aluminum surface treated with UED superhydrophobic coating for a set surface temperature of –8 °C and an average nozzle exit velocity of 2 m s^{-1}.

In the case of the aluminum surface treated with UED superhydrophobic coating, no adhesive detachment was observed on the surface for all flow velocities studied (see Figure 25). This is due to the roughness of the UED superhydrophobic surface, which is much greater than that of the PTFE-treated (hydrophobic) or untreated (hydrophilic) aluminum surfaces, as previously explained. However, after 9.91 seconds, a reduction in ice thickness was observed near the nozzle outlet due to ice crystal breakup within the ice layer (see Figure 28). This type of ice breakup is referred to as cohesive detachment, as the ice does not completely detach from the surface. Notably, the aluminum surface treated with the UED superhydrophobic coating exhibited higher ice adhesion compared to the aluminum treated with PTFE adhesive tape (hydrophobic) and untreated (hydrophilic).

4. Conclusions and outlook

In conclusion, this study aimed to understand the adhesion and detachment mechanisms of a 2 mm thick ice layer on different surfaces (hydrophilic, hydrophobic, and superhydrophobic) using a liquid jet with variable speeds under immersion conditions in a 10 wt.% ethanol/water mixture. The ultimate goal was to develop a method of ice slurry production without the need for mechanical scrapers. The key findings and implications of the study are summarized as follows:

1. Surface Temperature and Ice Growth: The study observed that the growth rate of the ice layer increased as the surface temperature decreased. Notably, the nature of the ice produced at different temperatures (−6 °C, −8 °C, and −9 °C) exhibited variations, with softer ice forming at −6 °C and −8 °C, which can easily disintegrate into ice particles, and harder ice forming at −9 °C, which is more resistant to disintegration into ice particles.
2. Surface Roughness and Ice Growth: The research revealed that increasing surface roughness created more nucleation sites, resulting in faster ice growth rates. Specifically, the superhydrophobic surface treated with UED exhibited the fastest ice growth, followed by the surface treated with PTFE, while the untreated aluminum surface showed the slowest growth.
3. Adhesion and Detachment Mechanisms: Surface roughness is a key factor influencing ice adhesion, as higher roughness leads to stronger mechanical adhesion of ice to surfaces. However, the case of aluminum surfaces treated with PTFE adhesive ribbon shows lower ice adhesion due to its low dielectric constant. The jet velocities required for soft ice detachment on the entire PTFE surface are two times lower than on untreated aluminum surfaces. This indicates that PTFE exhibits effective icephobic properties, reducing ice adhesion compared to untreated aluminum surfaces and those treated with superhydrophobic UED.
4. Modes of ice detachment: Adhesive detachment on low-roughness surfaces (untreated aluminum and PTFE adhesive tape-treated surfaces). Cohesive detachment on rougher surfaces, such as aluminum surfaces treated with UED superhydrophobic coating.

From a comprehensive perspective, applying a PTFE coating or adhesive ribbon to the ice slurry generator can reduce the energy required to remove ice from a surface. However, further investigation is needed to assess the durability and resistance of these coatings under low-temperature immersion conditions, especially when used in ice slurry generators for the food sector to ensure food safety. Moreover, future studies should examine ice adhesion on different surfaces using various methods such as centrifugation or shear, incorporating different mixtures to evaluate the effect of additives like ethanol and glycol in water on the nature of ice and its adhesion to surfaces.

Acknowledgements

The authors would like to thank the National Research Institute for Agriculture, Food, and the Environment (INRAE) and De Vinci Research Center (DVRC) for their financial support of ice slurry research.

References

[1] Z. Youssef, A. Delahaye, L. Huang, F. Trinquet, L. Fournaison, C. Pollerberg, C. Doetsch, State of the art on phase change material slurries, Energy Convers. Manag. 65 (2013) 120–132. https://doi.org/10.1016/j.enconman.2012.07.004.

[2] A.N. Leiper, E.C. Hammond, D.G. Ash, D.J. McBryde, G.L. Quarini, Energy conservation in ice slurry applications, Appl. Therm. Eng. 51 (2013) 1255–1262. https://doi.org/10.1016/j.applthermaleng.2012.11.044.

[3] P.W. Griffiths, P.C. Eames, Performance of chilled ceiling panels using phase change material slurries as the heat transport medium, Appl. Therm. Eng. 27 (2007) 1756–1760. https://doi.org/10.1016/j.applthermaleng.2006.07.009.

[4] A. Kumar, S.K. Yadav, A. Mahato, A. Kumar, On-demand intermittent ice slurry generation for subzero cold thermal energy storage: Numerical simulation and performance analysis, Appl. Therm. Eng. 161 (2019) 114081. https://doi.org/10.1016/j.applthermaleng.2019.114081.

[5] J. Bellas, I. Chaer, S.A. Tassou, Heat transfer and pressure drop of ice slurries in plate heat exchangers, Appl. Therm. Eng. 22 (2002) 721–732. https://doi.org/10.1016/S1359-4311(01)00126-0.

[6] V. Kapsalis, D. Karamanis, Solar thermal energy storage and heat pumps with phase change materials, Appl. Therm. Eng. 99 (2016) 1212–1224. https://doi.org/10.1016/j.applthermaleng.2016.01.071.

[7] P.W. Egolf, M. Kauffeld, From physical properties of ice slurries to industrial ice slurry applications, Int. J. Refrig. 28 (2005) 4–12. https://doi.org/10.1016/j.ijrefrig.2004.07.014.

[8] I. Dincer, M.A. Rosen, Thermal energy storage: systems and applications, John Wiley & Sons, 2021.

[9] F. Afsharpanah, K. Pakzad, S.S. Mousavi Ajarostaghi, M. Arıcı, Assessment of the charging performance in a cold thermal energy storage container with two rows of serpentine tubes and extended surfaces, J. Energy Storage. 51 (2022) 104464. https://doi.org/10.1016/j.est.2022.104464.

[10] F. Afsharpanah, S.S. Mousavi Ajarostaghi, M. Arıcı, Parametric study of phase change time reduction in a shell-and-tube ice storage system with anchor-type fin design, Int. Commun. Heat Mass Transf. 137 (2022) 106281. https://doi.org/10.1016/j.icheatmasstransfer.2022.106281.

[11] F. Afsharpanah, M. Izadi, F.A. Hamedani, S.S. Mousavi Ajarostaghi, W. Yaïci, Solidification of nano-enhanced PCM-porous composites in a cylindrical cold thermal energy storage enclosure, Case Stud. Therm. Eng. 39 (2022) 102421. https://doi.org/10.1016/j.csite.2022.102421.

[12] M. Kauffeld, M.J. Wang, V. Goldstein, K.E. Kasza, Ice slurry applications, Int. J. Refrig. 33 (2010) 1491–1505. https://doi.org/10.1016/j.ijrefrig.2010.07.018.

[13] E. Stamatiou, J.W. Meewisse, M. Kawaji, Ice slurry generation involving moving parts, Int. J. Refrig. 28 (2005) 60–72. https://doi.org/10.1016/j.ijrefrig.2004.07.016.

[14] W. Samah, P. Clain, F. Rioual, L. Fournaison, A. Delahaye, Review on ice crystallization and adhesion to optimize ice slurry generators without moving components, Appl. Therm. Eng. (2023) 119974. https://doi.org/10.1016/j.applthermaleng.2023.119974.

[15] M.B. Lakhdar, R. Cerecero, G. Alvarez, J. Guilpart, D. Flick, A. Lallemand, Heat transfer with freezing in a scraped surface heat exchanger, Appl. Therm. Eng. 25 (2005) 45–60. https://doi.org/10.1016/j.applthermaleng.2004.05.007.

[16] M.N.A. Hawlader, M.A. Wahed, Analyses of ice slurry formation using direct contact heat transfer, Appl. Energy. 86 (2009) 1170–1178. https://doi.org/10.1016/j.apenergy.2008.11.003.

[17] Y. Gao, Y. Ning, C. Wu, M. Xu, S. Akhtar, A.S. Mujumdar, A.P. Sasmito, Experimental investigation of producing ice slurry with water using opposed-nozzle impinging jet method, Appl. Therm. Eng. (2022) 119568. https://doi.org/10.1016/j.applthermaleng.2022.119568.

[18] H.T. Shin, Y.P. Lee, J. Jurng, Spherical-shaped ice particle production by spraying water in a vacuum chamber, Appl. Therm. Eng. 20 (2000) 439–454. https://doi.org/10.1016/S1359-4311(99)00035-6.

[19] M. Barth, Procede pour detacher les cristaux de glace d'un echangeur thermique generateur d'un frigoporteur diphasique liquide-solide, EP1101071B1, 2000. https://patentscope.wipo.int/search/fr/detail.jsf?docId=WO2000071945.

[20] S. Brooks, M. Tierney, G. Quarini, Experimental investigation of different materials for use in ice slurry generation, Int. J. Refrig. 129 (2021) 97–108. https://doi.org/10.1016/j.ijrefrig.2021.05.019.

[21] S. Brooks, G. Quarini, M. Tierney, X. Yun, E. Lucas, Conditions for continuous ice slurry generation in a nylon helical coiled heat exchanger, Therm. Sci. Eng. Prog. 15 (2020) 100427. https://doi.org/10.1016/j.tsep.2019.100427.
[22] Y. Zhao, Z. Li, Y. Utaka, Z. Chen, H. Ohkubo, Adhesion characteristics of ice in urea aqueous solution for efficient slurry formation in cold storage, Int. J. Refrig. 100 (2019) 335–342. https://doi.org/10.1016/j.ijrefrig.2019.01.020.
[23] H. Wang, R. Feng, H. Duan, A. Chen, Study on sub-cooler based on the characteristics of the super-hydrophobic surface, Exp. Therm. Fluid Sci. 76 (2016) 205–210. https://doi.org/10.1016/j.expthermflusci.2016.03.023.
[24] H. Wang, G. He, Q. Tian, Effects of nano-fluorocarbon coating on icing, Appl. Surf. Sci. 258 (2012) 7219–7224. https://doi.org/10.1016/j.apsusc.2012.04.043.
[25] H. Wang, G. He, Q. Tian, Experimental study of the supercooling heat exchanger coated with fluorocarbon coating, Energy Build. 55 (2012) 526–532. https://doi.org/10.1016/j.enbuild.2012.09.012.
[26] H. Wang, Y. Wang, The flow and heat transfer characteristics of supercooled water based on the nano-superhydrophobic surface, Heat Mass Transf. 55 (2019) 413–420. https://doi.org/10.1007/s00231-018-2424-1.
[27] H. Wang, G. He, R. Feng, An effective method for preventing ice-blockage in dynamic generation system with supercooling water, Int. J. Refrig. 46 (2014) 114–122. https://doi.org/10.1016/j.ijrefrig.2014.05.010.
[28] W. Samah, P. Clain, F. Rioual, L. Fournaison, A. Delahaye, Experimental investigation on the wetting behavior of a superhydrophobic surface under controlled temperature and humidity, Colloids Surf. Physicochem. Eng. Asp. 656 (2023) 130451. https://doi.org/10.1016/j.colsurfa.2022.130451.
[29] W. Samah, P. Clain, L. Fournaison, F. Rioual, A. Delahaye, Étude du comportement de mouillage d'une goutte d'eau sur une surface superhydrophobe en fonction de la température et de l'humidité, Congrès Annu. Société Fr. Therm. 2022 Valenciennes Fr. (2022) 10. https://doi.org/10.25855/SFT2022-045.
[30] D. Carbonell, M. Schubert, J.R. Frandsen, J. Brand, K. Erb, L. Laib, M. Munari, Development of supercoolers for ice slurry generators using icephobic coatings., Int. J. Refrig. 144 (2022) 90–98. https://doi.org/10.1016/j.ijrefrig.2022.07.011.
[31] A. Bey, M.A.A. Faruque, R. Balachandar, Effects of varying submergence and channel width on local scour by plane turbulent wall jets, J. Hydraul. Res. 46 (2008) 764–776. https://doi.org/10.1080/00221686.2008.9521921.
[32] A. Nasr, J.C.S. Lai, A turbulent plane offset jet with small offset ratio, Exp. Fluids. 24 (1998) 47–57. https://doi.org/10.1007/s003480050149.
[33] X. Li, M. Zhou, J. Zhang, W. Xu, Numerical Study of the Velocity Decay of Offset Jet in a Narrow and Deep Pool, Water. 11 (2018) 59. https://doi.org/10.3390/w11010059.
[34] S. Nishimoto, B. Bhushan, Bioinspired self-cleaning surfaces with superhydrophobicity, superoleophobicity, and superhydrophilicity, RSC Adv. 3 (2012) 671–690. https://doi.org/10.1039/C2RA21260A.
[35] X. Huang, N. Tepylo, V. Pommier-Budinger, M. Budinger, E. Bonaccurso, P. Villedieu, L. Bennani, A survey of icephobic coatings and their potential use in a hybrid coating/active ice protection system for aerospace applications, Prog. Aerosp. Sci. 105 (2019) 74–97. https://doi.org/10.1016/j.paerosci.2019.01.002.
[36] L. Cao, A.K. Jones, V.K. Sikka, J. Wu, D. Gao, Anti-Icing Superhydrophobic Coatings, Langmuir. 25 (2009) 12444–12448. https://doi.org/10.1021/la902882b.
[37] P. Du, J. Wen, Z. Zhang, D. Song, A. Ouahsine, H. Hu, Maintenance of air layer and drag reduction on superhydrophobic surface, Ocean Eng. 130 (2017) 328–335. https://doi.org/10.1016/j.oceaneng.2016.11.028.
[38] H.D.B.S. Heorton, N. Radia, D.L. Feltham, A Model of Sea Ice Formation in Leads and Polynyas, J. Phys. Oceanogr. 47 (2017) 1701–1718. https://doi.org/10.1175/JPO-D-16-0224.1.

[39] S. Rønneberg, J. He, Z. Zhang, The need for standards in low ice adhesion surface research: a critical review, J. Adhes. Sci. Technol. 34 (2020) 319–347. https://doi.org/10.1080/01694243.2019.1679523.
[40] M. Rouaud, Calcul d'incertitudes: application aux sciences expérimentales exercices corrigés, Mathieu Rouaud, Querrien, 2014.
[41] J. Chen, J. Liu, M. He, K. Li, D. Cui, Q. Zhang, X. Zeng, Y. Zhang, J. Wang, Y. Song, Superhydrophobic surfaces cannot reduce ice adhesion, Appl. Phys. Lett. 101 (2012) 111603. https://doi.org/10.1063/1.4752436.
[42] S.A. Kulinich, M. Farzaneh, How Wetting Hysteresis Influences Ice Adhesion Strength on Superhydrophobic Surfaces, Langmuir. 25 (2009) 8854–8856. https://doi.org/10.1021/la901439c.
[43] J. Jiang, Q. Sheng, G.H. Tang, M.Y. Yang, L. Guo, Anti-icing propagation and icephobicity of slippery liquid-infused porous surface for condensation frosting, Int. J. Heat Mass Transf. 190 (2022) 122730. https://doi.org/10.1016/j.ijheatmasstransfer.2022.122730.
[44] S. Lei, X. Fang, J. Ou, F. Wang, M. Xue, W. Li, A. Amirfazli, S.F. Chini, Icing of static and high-speed water droplets on superhydrophobic surface, Mater. Lett. 285 (2021) 129048. https://doi.org/10.1016/j.matlet.2020.129048.
[45] M. Zou, S. Beckford, R. Wei, C. Ellis, G. Hatton, M.A. Miller, Effects of surface roughness and energy on ice adhesion strength, Appl. Surf. Sci. 257 (2011) 3786–3792. https://doi.org/10.1016/j.apsusc.2010.11.149.
[46] Z. He, S. Xiao, H. Gao, J. He, Z. Zhang, Multiscale crack initiator promoted super-low ice adhesion surfaces, Soft Matter. 13 (2017) 6562–6568. https://doi.org/10.1039/C7SM01511A.
[47] M. Landy, A. Freiberger, Studies of ice adhesion: I. Adhesion of ice to plastics, J. Colloid Interface Sci. 25 (1967) 231–244. https://doi.org/10.1016/0021-9797(67)90026-4.
[48] L. Lliboutry, The crystalline texture and plastic deformation of ice, J. Hydraul. Res. 2 (1964) 41–49. https://doi.org/10.1080/00221686409500071.
[49] R.M. Fillion, A.R. Riahi, A. Edrisy, Design factors for reducing ice adhesion, J. Adhes. Sci. Technol. 31 (2017) 2271–2284. https://doi.org/10.1080/01694243.2017.1297588.
[50] R. Menini, M. Farzaneh, Elaboration of Al2O3/PTFE icephobic coatings for protecting aluminum surfaces, Surf. Coat. Technol. 203 (2009) 1941–1946. https://doi.org/10.1016/j.surfcoat.2009.01.030.

Appendix A: Measurement uncertainty of liquid jet velocity and ice detachment length (L_D) for the case of untreated aluminum surface.

The data related to the liquid jet velocity and ice detachment length (L_D) from Figure 22, which represents the evolution of the average ice detachment length L_D as a function of the average velocity at the nozzle outlet in the case of an untreated aluminum surface, are detailed in Tables A1, A2, and A3, along with their absolute uncertainties. The data are provided for each studied surface temperature (–6 °C, –8 °C, and –9 °C).

Table A.1: *Absolute uncertainties of the measurements of liquid jet velocities and ice detachment lengths (L_D) for the case of the untreated aluminum surface temperature of –6 °C.*

Untreated aluminum surface temperature of –6°C			
Average liquid jet velocity ($m\ s^{-1}$)	Absolute uncertainty of the liquid jet velocity ($m\ s^{-1}$)	Average ice detachment length L_D (m)	Absolute uncertainty of ice detachment length L_D (m)
0.51	±0.062	0	0
0.64	±0.004	0.031	±0.0016
0.81	±0.0155	0.059	±0.0037
1.11	±0.042	0.094	±0.0038
1.39	±0.031	0.116	±0.0027
1.60	±0.085	0.129	±0.0046
1.90	±0.03	0.139	±0.0012
2.03	±0.062	0.149	±0.0027
2.45	±0.0134	0.160	0

Table A.2: *Absolute uncertainties of the measurements of liquid jet velocities and ice detachment lengths (L_D) for the case of the untreated aluminum surface temperature of –8 °C.*

Untreated aluminum surface temperature of –8 °C			
Average liquid jet velocity ($m\ s^{-1}$)	Absolute uncertainty of the liquid jet velocity ($m\ s^{-1}$)	Average ice detachment length L_D (m)	Absolute uncertainty of ice detachment length L_D (m)
0.64	±0.008	0	0
0.83	±0.016	0.036	±0.0056
1.09	±0.075	0.063	±0.0023
1.41	±0.087	0.080	±0.0078
1.62	±0.046	0.094	±0.0035
1.87	±0.07	0.115	±0.0013
2.04	±0.065	0.125	±0.0071
2.45	±0.0052	0.149	±0.0026
2.84	±0.026	0.160	0

Table A.3: *Absolute uncertainties of the measurements of liquid jet velocities and ice detachment lengths (L_D) for the case of the untreated aluminum surface temperature of –9 °C.*

Untreated aluminum surface temperature of –9 °C			
Average liquid jet velocity (m s^{-1})	Absolute uncertainty of the liquid jet velocity (m s^{-1})	Average ice detachment length L_D (m)	Absolute uncertainty of ice detachment length L_D (m)
1.08	±0.005	0	0
1.40	±0.034	0.034	±0.0026
1.61	±0.111	0.066	±0.0214
1.89	±0.07	0.091	±0.0054
2.13	±0.052	0.106	±0.0095
2.45	±0.075	0.124	±0.0060
2.85	±0.025	0.134	±0.0067

Appendix B: Measurement uncertainty of liquid jet velocity and ice detachment length (L_D) for aluminum surfaces treated with PTFE adhesive tape and for aluminum surfaces treated with UED.

The data related to the average liquid jet velocity and average ice detachment length (L_D) from Figure 25 are provided for the case of aluminum surfaces treated with PTFE adhesive tape, as well as for the case of aluminum surfaces treated with the Ultra Ever Dry (UED) coating (superhydrophobic). The data, along with their absolute uncertainties, are detailed in Tables B1 and B2 for the surface temperature case studied, –8 °C.

Table B.1: *Absolute uncertainties of the measurements of liquid jet velocities and ice detachment lengths (L_D) for the case of aluminum surfaces treated with PTFE adhesive tape with a surface temperature set at –8 °C.*

Aluminum surfaces treated with PTFE adhesive tape			
Average liquid jet velocity (m s^{-1})	Absolute uncertainty of the liquid jet velocity (m s^{-1})	Average ice detachment length L_D (m)	Absolute uncertainty of ice detachment length L_D (m)
0.15	±0.013	0	0
0.38	±0.051	0.032	±0.0102
0.63	±0.034	0.055	±0.0053
0.84	±0.034	0.079	±0.0028
1.11	±0.05	0.119	±0.0109
1.37	±0.08	0.160	0

Table B.2: *Absolute uncertainties of the measurements of liquid jet velocities and ice detachment lengths (L_D) for the case of aluminum surfaces treated with the Ultra Ever Dry (UED) coating (superhydrophobic) with a surface temperature set at –8 °C.*

Aluminum surfaces treated with the Ultra Ever Dry (UED) coating			
Average liquid jet velocity ($m\ s^{-1}$)	Absolute uncertainty of the liquid jet velocity ($m\ s^{-1}$)	Average ice detachment length L_D (m)	Absolute uncertainty of ice detachment length L_D (m)
0.30	±0.002	0	0
0.40	±0.003	0	0
0.50	±0.003	0	0
0.84	±0.008	0	0
1.09	±0.003	0	0
1.35	±0.075	0	0
1.54	±0.165	0	0
1.93	±0.005	0	0
2.04	±0.07	0	0
2.45	±0.026	0	0
2.85	±0.034	0	0

Context

Scraped surface generators are the most commonly used in the refrigeration industry for ice slurry production.

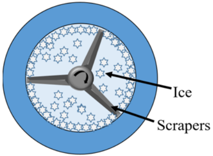

These scraped surface ice slurry generators have drawbacks due to the adhesive strength of the ice:

❖Excessive consumption of additional mechanical energy.

❖High investment costs.

❖Wearing out of the scrapers.

Reduction of ice adhesion for optimization of ice slurry generators

❖ Use of additives to form a soft, porous ice layer to reduce ice adhesion.

❖ Surface modification: reduction of roughness and/or use of low surface energy coatings to reduce the adhesion force of the soft ice to the generator surface and facilitate its detachment only by liquid flow (hydro scraping).

❖ Use of an intermittent liquid jet to detach the soft ice layer after the formation of a thin layer of 1 to 2 mm.